

# Meteosat SEVIRI Fire Radiative Power (FRP) Products from the Land Surface Analysis Satellite Applications Facility (LSA SAF): Part 1 - Algorithms, Product Contents & Analysis

Wooster, M.J.<sup>1,2</sup>, Roberts, G.<sup>3</sup>, Freeborn, P. H.<sup>1,4</sup>, Xu, W.<sup>1</sup>, Govaerts, Y.<sup>5</sup>, Beeby, R.<sup>1</sup>,  
He, J.<sup>1</sup>, A. Lattanzio<sup>6</sup>, Fisher, D.<sup>1,2</sup>, and Mullen, R.<sup>1</sup>.

<sup>1</sup> King's College London, Environmental Monitoring and Modelling Research Group,  
Department of Geography, Strand, London, WC2R 2LS, UK.

<sup>2</sup> NERC National Centre for Earth Observation (NCEO), UK.

<sup>3</sup> Geography and Environment, University of Southampton, Highfield, Southampton  
SO17 1BJ, UK.

<sup>4</sup> Fire Sciences Laboratory, Rocky Mountain Research Station, U.S. Forest Service,  
Missoula, Montana, USA.

<sup>5</sup> Rayference, Brussels, Belgium.

<sup>6</sup> MakaluMedia, Darmstadt, Germany

## Abstract

Characterising changes in landscape fire activity at better than hourly temporal resolution is achievable using thermal observations of actively burning fires made from geostationary Earth observation (EO) satellites. Over the last decade or more, a series of research and/or operational 'active fire' products have been developed from geostationary EO data, often with the aim of supporting biomass burning fuel consumption and trace gas and aerosol emission calculations. Such "Fire Radiative Power" (FRP) products are generated operationally from Meteosat by the Land Surface Analysis Satellite Applications Facility (LSA SAF), and are available freely every 15 minutes in both near real-time and archived form. These products map the location of actively burning fires and characterise their rates of thermal radiative energy release (fire radiative power; FRP), which is believed proportional to rates of biomass consumption and smoke emission. The FRP-PIXEL Product contains the full spatio-temporal resolution FRP dataset derivable from the SEVIRI imager onboard Meteosat at a 3 km spatial sampling distance (decreasing away from the west African sub-satellite point), whilst the FRP-GRID product is an hourly summary at 5° grid resolution that includes simple bias adjustments for meteorological cloud cover and regional underestimation of FRP caused primarily by under-detection of low FRP fires. Here we describe the enhanced geostationary Fire Thermal Anomaly (FTA) detection algorithm used to deliver these products, and detail the methods used generate the atmospherically corrected FRP and per-pixel uncertainty metrics. Using SEVIRI scene simulations and real SEVIRI data, including from a period of Meteosat-8 'special operations', we describe certain sensor and data pre-processing characteristics that influence SEVIRI's active fire detection and FRP measurement

44 capability, and use these to specify parameters in the FTA algorithm and to make  
45 recommendations for the forthcoming Meteosat Third Generation operations in  
46 relation to active fire measures. We show that the current SEVIRI FTA algorithm is  
47 able to discriminate actively burning fires covering down to  $10^{-4}$  of a pixel, and that it  
48 appears more sensitive to fire than are algorithms used to generate many other widely  
49 exploited active fire products. Finally, we briefly illustrate the information contained  
50 within the current Meteosat FRP-PIXEL and FRP-GRID products, providing example  
51 analyses for both individual fires and multi-year regional-scale fire activity, whilst the  
52 companion paper (Roberts *et al.*, 2015) provides a full product performance  
53 evaluation and a demonstration of product use within components of the Copernicus  
54 Atmosphere Service (CAMS).

## 1. INTRODUCTION

### 1.1. Meteosat Second Generation and Biomass Burning Observations

Smoke emissions from landscape scale fires are strong influencers of atmospheric composition, chemistry and climate (Williams *et al.*, 2010), and Earth Observation (EO) satellites are key to their characterisation. The European Organisation for the Exploitation of Meteorological Satellites (EUMETSAT) currently operates the Meteosat Second Generation (MSG) system, Europe's geostationary EO programme for studying weather, climate and the Earth environment. Meteosat carries the Spinning Enhanced Visible and Infrared Imager (SEVIRI), whose data can be used to detect actively burning fires and to estimate their Fire Radiative Power (FRP). FRP has been shown in laboratory and field experiments to be proportional to rates of fuel consumption and smoke production (Wooster *et al.* 2005; Freeborn *et al.* 2008; Kremens *et al.* 2012; Pereira *et al.* 2011). Since the first MSG launch in 2002, SEVIRI has observed Europe, Africa, and parts of South America every 15 minutes, and provided the first geostationary EO data to be used to estimate FRP from landscape fires (Roberts *et al.* 2005; Wooster *et al.* 2005; Roberts and Wooster 2008). SEVIRI-derived FRP data have been used to parameterise high temporal resolution smoke emissions fields for atmospheric modelling (Baldassarre *et al.*, 2014), including within the Copernicus Atmosphere Monitoring Service (CAMS, Roberts *et al.*, this issue). Here we describe the algorithms and characteristics of the SEVIRI FRP products available operationally from the EUMETSAT Land Surface Analysis Satellite Applications Facility (LSA SAF; <http://landsaf.ipma.pt>). These products are available via both near-real time and offline dissemination routes, and have already provided information used in a number of biomass burning emissions inventories (e.g. Turquety *et al.*, 2014), and to the Global Fire Assimilation System (GFAS) that provides fire emissions data to the CAMS (e.g. Hollingsworth *et al.*, 2008; Kaiser *et al.*, 2012; Andela *et al.*, 2015).

### 1.2. Landscape Scale Fires and Smoke Emissions

Including a sufficiently accurate spatio-temporal description of landscape fire emissions is a fundamental pre-requisite for certain atmospheric 'information services', including those aimed at studying long-range transport of air pollutants (Reid *et al.* 2009), the near-real time monitoring and forecasting of air quality (e.g. Sofiev *et al.* 2009; Kaiser *et al.* 2012) and the determination of atmospheric composition variations (Clerbaux *et al.*, 2009; Ross *et al.* 2013). Furthermore, carbon accounting parameters derived from EO-derived FRP data are contributing to long-term regional and global biomass burning emissions inventories (e.g. Remy and Kaiser 2014; Roberts *et al.* 2011; Vermote *et al.* 2009; Zhang *et al.* 2012), which in turn can be used to gauge compliance with international treaties on greenhouse gas

(GHG) and air pollutant emission ceilings. In this context, the type of very high temporal resolution active fire information available operationally in near real-time from SEVIRI (Figure 1a) are very complementary to the higher spatial resolution, but more temporally limited, views of the same fires available from polar orbiters (Figure 1b) (e.g. Giglio *et al.* 2003; Wooster *et al.*; 2012; Schroeder *et al.*, 2014). A high temporal resolution view is particularly useful because fires generally show substantial short term activity variations and radical diurnal shifts in behaviour (Roberts *et al.*, 2009a; Andela *et al.*, 2015). Rapidly supplied, regularly updated active fire information can even provide useful information for early warning and near-continuous tracking of new fire activity (e.g. Dlamini, 2007).

Using an operational version of the geostationary Fire Thermal Anomaly (FTA) algorithm of Roberts and Wooster (2008), the MSG satellites provide high temporal resolution FRP data relating to fires burning across the African and European continents, and also the eastern edge of South America (see Supplement Figure S1 for the Meteosat Disk). Africa is considered the most 'fire affected' continent, responsible for ~ 30 - 50% of global burned area and a very significant proportion of annual global fire emissions (Andreae 1991; van der Werf *et al.* 2003; 2006). Landscape burning is also relatively common across parts of Europe, and occasionally extreme 'wildfire' outbreaks can threaten large population centres and/or deliver acute air quality impacts, particularly in southern Europe (Liu *et al.*, 2009; Baldassarre *et al.*, 2015; Roberts *et al.*, 2015). The region of South America viewed by SEVIRI is primarily dry and moist forest, cerrado and croplands, which is also greatly fire affected, but because of the extreme SEVIRI view angles the FTA algorithm applied to the GOES Imager provides better geostationary FRP data here (Xu *et al.*, 2010).

### 1.3. LSA SAF Meteosat SEVIRI FRP Products

Two Meteosat SEVIRI FRP products are delivered operationally in near real-time and archived form by the EUMETSAT LSA SAF (<http://landsaf.ipma.pt>) whose mission is described in Trigo *et al.* (2011). These are the Level 2 FRP-PIXEL product, delivered at SEVIRI's full spatial and temporal resolution, and the Level 3 spatio-temporal summary FRP-GRID product. Here we document the algorithms and information content relevant to both products, focusing in particular on enhancements made to the prototype FTA algorithm first described in Roberts and Wooster (2008) and also to the retrieval of FRP and its associated uncertainties. We illustrate how the SEVIRI pre-processing chain influences these retrievals, and demonstrate differences between the FRP-PIXEL and an alternative active fire product (WFABBA-SEVIRI) also being generated from SEVIRI observations. The companion paper (Roberts *et al.*, 2015) provides detailed product performance evaluation, a much more extensive SEVIRI Fire Product intercomparison, and a demonstration of use of the FRP-PIXEL product in the characterisation of fire emissions within the Copernicus Atmosphere Monitoring Service (CAMS). Finally we provide recommendations for pre-processing considerations related to Meteosat Third Generation observations of active fires.



## **2. OVERVIEW OF THE LSA SAF FIRE RADIATIVE POWER (FRP) PRODUCT GENERATION**

### **2.1 Active Fire Data from the MSG Satellite Series**

There are a total of four spin-stabilised MSG satellites in orbit (Meteosat 8 to 11), launched in 2002, 2005, 2012 and 2015 respectively. Each rotates at a speed of 100 rpm and provides Earth images from the SEVIRI spin scan radiometer (Aminou *et al.*, 1997; Aminou, 2002). The primary full Earth disk MSG observatory is located at 0° longitude, whilst the others provide Rapid Scanning Services over a reduced fraction of the Earth disk and/or backup capabilities.

SEVIRI operates in 12 spectral channels (Aminou *et al.* 1997), and the fact that the mid-wave infrared (MWIR: IR3.9) and longwave infrared (LWIR: IR10.8 and IR12.0) bands (Channels 4, 9 and 10 in Table 1) are differently sensitive to the thermal radiance emitted by high temperature sources (e.g. Prins *et al.* 1998) allows SEVIRI in theory to detect actively burning fires covering as little as  $10^{-4}$  of a pixel (Roberts *et al.*, 2005; Wooster *et al.*, 2013). However, the FTA algorithm must take care to prevent sunglint and other potentially confounding features being falsely identified as active fires, and this requires use of data from other SEVIRI spectral channels (Section 3). Confirmed active fire pixels have their FRP estimated using the MIR radiance method of Wooster *et al.* (2003; 2005; Section 4), with delivery of a full per-pixel FRP uncertainty measure provided using methods outlined in Section 5.

### **2.2. SEVIRI Data Capture and Pre-processing**

As the Meteosat satellite spins (east-to-west), SEVIRI's scan mirror is stepped (south-to-north) to build up an image of the full Earth disk over a period of ~ 12.5 minutes (Aminou, 2002). The full repeat cycle is ~15 min, though shorter if only part of the Earth disk is imaged. SEVIRI's diamond shaped pixels have an instantaneous field of view (IFOV) of 4.8 km × 4.8 km at the west African sub-satellite point (SSP), with an SSP ground sampling distance of 3 km (full width at half maximum; FWHM) and a final image resolution of around 6 km (Just, 2000; Aminou, 2002; Schmetz *et al.*, 2002; Calle *et al.* 2009). These distances increase with view zenith angle, yielding larger and more widely separated ground footprints further from the SSP.

SEVIRI data are transmitted from the MSG satellites to the Primary Ground Station (PGS) in Usingen (Germany), and then sent to the Image Processing Facility (IMPF) at Darmstadt (Just 2000; Murphy, 2013) to be radiometrically/geometrically corrected and geolocated from level 1.0 to level 1.5. They are then forwarded to users, including the LSA SAF headquartered at the Instituto Portugues do Mar e da Atmosfera in Portugal (DaCamara, 2006; Trigo *et al.*, 2011).

### **2.3. Introduction to the LSA SAF Meteosat SEVIRI FRP Product Suite**

As with all other current Level 2 LSA SAF products (Trigo *et al.*, 2011) the FRP-PIXEL product is currently generated separately for the four geographic regions of the Meteosat disk: Europe (Euro), Northern Africa (NAfr), Southern Africa (SAfr), and South America (Same) (see Supplement Figure S1), though this split dissemination will soon be replaced by the delivery of full disk Level 2 products. The Level 3 FRP-GRID product is already full disk, albeit at a reduced spatio-temporal resolution, and includes simple adjustments for cloud cover and for SEVIRI's inability to detect the lowest FRP fires (Freeborn *et al.*, 2009),

Each FRP-PIXEL product actually consists of two separate product files: (i) an 'FRP-PIXEL List Product' file that stores variables derived at each detected active fire pixel, and (ii) an 'FRP-PIXEL Quality Product' file that contains a 2D array of flags recording the processing status of each SEVIRI pixel, not just those identified as containing active fires (e.g. whether the FTA algorithm classified a pixel as water, cloud contaminated, sun glint-affected, cloud-free but with no fires, or was classed as a confirmed 'true' active fire pixel etc). The Quality Product codes are shown in Table S1 of the Supplement, which also includes further details on product structure and accessibility (as does <http://landsaf.ipma.pt>).

Because the FRP-PIXEL product files are able to be delivered to users within one hour of image acquisition, and are thus more frequent and more timely than most other EO active fire products, they can capture the high frequency FRP fluctuations shown by landscape scale fires and may meet some of the demands for "rapid response/decision support" fire products (Frost and Annegarn, 2007). Figure 2 illustrates one example of the spatio-temporal distribution of active fire data extracted from the 96 FRP-PIXEL List Product files covering southern Africa during a single day. Freeborn *et al.* (2014a) recently demonstrated that over regions of Central Africa, the FTA algorithm successfully detects fire pixels having an FRP down to around 10 MW. However, below around 30-40 MW active fire pixel counts are increasingly underestimated due to the difficulty in detecting these lower FRP fire pixels within the relatively coarse SEVIRI pixels, and Figure 2 indicates very low numbers of fire pixels with an FRP less than 25 MW are detected on this day. Adjustments are applied in the FRP Grid Product to account for this effect and thus better estimate landscape-scale regional FRP totals (Section 6).

### **3. OPERATIONAL IMPLEMENTATION OF THE GEOSTATIONARY FIRE THERMAL ANOMALY (FTA) ALGORITHM**

#### **3.1. The FRP-PIXEL Product Processing Chain**

The LSA SAF FRP Product processing chain (Figure 3) ingests level 1.5 SEVIRI data calibrated into  $\text{mW.m}^{-2}.\text{sr}^{-1}.\text{(cm}^{-1})^{-1}$ , and also into kelvins for the infrared channels. The online Algorithm Theoretical Basis Document (ATBD) available at <http://landsaf.ipma.pt> provides full details, whereas we provide here the key features

and operational enhancements made beyond the Roberts and Wooster (2008) FTA algorithm prototype.

### 3.2. Pre-Processing Stage: Water, Cloud and Smoke Discrimination

Sunglints from water can result in false active fire detections (Zhukov *et al.*, 2006), so SEVIRI pixels containing major water bodies are masked using the 1 km Global Land Cover (GLC 2000) map of Mayaux *et al.* (2004). Clouds can cause similar problems, and may also contaminate the background window characteristics used in the "contextual" active fire pixel confirmation stage (Section 3.5), but smoke need not be masked since active fires often remain highly detectable through smoke (Libonati *et al.* 2010). LSA SAF processing currently uses the Nowcasting and Very Short Range Forecasting SAF (NWC SAF; [www.nwcsaf.org](http://www.nwcsaf.org)) cloud mask (CMA; Derrien and Le Gleau, 2005), with CMA pixels reclassified as non-cloudy for the fire application if their cloudy classification is based on either of the following tests, which are fully detailed in Derrien and Le Gleau (2005) and MeteoFrance (2010):

(i) the Local Spatial Texture test, applied to a  $3 \times 3$  pixel window to detect broken clouds/cloud edges by exploiting the higher spatial variations typical of visible ( $0.6 \mu\text{m}$ ), NIR ( $0.8 \mu\text{m}$ ) and/or LWIR channel measures around such features. Areas of active fire and smoke often show similar spatial variations, so the test is inappropriate here.

(ii) the Brightness Temperature Difference (BTD;  $BT_{3.9} - BT_{10.8}$ ) test, which detects semi-transparent clouds at night and low-level clouds during the day, exploiting the lower water cloud emissivity in the SEVIRI IR3.9 channel as compared to the IR10.8 channel. BTD increases over active fires and so a CMA BTD classified pixel only remains as cloudy if it passes the following three conditions:

$$BT_{3.9} - BT_{10.8} > 6.0 \text{ K} \quad (1)$$

$$BT_{10.8} - BT_{12.0} > 1.5 \text{ K} \quad (2)$$

$$\frac{L_{3.9}}{L_{0.64}} < 0.7 \quad (3)$$

where  $BT_{3.9}$ ,  $BT_{10.8}$ , and  $BT_{12.0}$  are the pixel brightness temperatures in the SEVIRI IR3.9 (MWIR), IR10.8  $\mu\text{m}$  (LWIR) and IR12.0  $\mu\text{m}$  (LWIR) channels respectively, and  $L_{3.9}$  and  $L_{0.64}$  are the spectral radiances in the IR3.9 and VIS0.6  $\mu\text{m}$  (visible) channels respectively (see Table 1).

(iii) The Spatial Smoothing test, which fills in cloud detection 'gaps' in areas of semi-transparent cloud. If at least three pixels immediately surrounding a cloudy pixel were classed as cloudy based on this test, then the pixel is reclassified as non-cloudy.

CMA cloud mask pixels remaining after the above adjustments are assigned Class 3 ('Cloud') in the FRP-PIXEL Quality Product (Supplement Table S1). As an indication of the importance of our CMA cloud mask adaptations, one day of SEVIRI data of southern Africa (7 July 2004) was processed using both the standard and adjusted CMA masks, and was found to show 22% fewer 'confirmed' active fire pixels in the former case. However, despite the adjusted CMA mask being far better suited to FRP product cloud screening, Freeborn *et al.* (2014a) demonstrate that its performance substantially differs from that of the simpler masks used, for example, within the MODIS MOD14/MYD14 Active Fire and Thermal Anomaly products (Giglio *et al.*, 2003). For example, whilst the adjusted SEVIRI CMA masks thinly and partially cloud-covered pixels, the MOD14/MYD14 product often allows fire detection in such areas (Figure 4), albeit the retrieved FRP values maybe perturbed. To assess the potential for the retrieval of FRP values under thinly and/or partially cloud covered SEVIRI pixels, an analysis was made using an additional 'cloud type' mask where cloudy pixels are further classified according to their optical characteristics obtained from the NWC SAF cloud type product (CT; Derrien and Le Gleau, 2005). For this analysis, five days of SEVIRI data over Southern Africa were processed using the FTA algorithm and potential active fire pixels split into two classes: in clear sky or under optically thin cloud cover (overlying CT mask values of 15, 16, 17 or 19). Following the standard processing of the potential active fire pixels as shown in Figure 3, it was found that only ~0.01% of those under the optically thin cloud cover were finally classed as confirmed fire pixels. This was initially assumed to be due to the sunglint screening employed by the FTA algorithm, since cloud contaminated pixels typically exhibit increased radiances in visible channels, leading to their rejection in the MIR/RED ratio test (Section 3.4). However, when the sunglint screening tests were removed similar results were obtained, with the almost all potential active fire pixels being instead rejected at the background characterisation step (Section 3.5), i.e. too few suitable background pixels were located in regions of optically thin cloud to effectively characterise the potential fire pixel background. Figure 5 shows boxplots of the mean background and potential fire pixel IR3.9 BT and IR3.9 - IR10.9 BT difference for this dataset. Under clear sky conditions, the median IR3.9BT for potential active fire pixels is 306.2 K and for the background 303.4 K. Under optically thin cloud these values lower to 298.9 K and 298.1 K respectively, and the difference between the IR3.9BT of fire and non-fire pixels thus generally reduces. For the BT difference, the median potential active fire pixel signal under clear sky is 4.2 K, and the background 2.2 K. Under optically thin cloud these increase to 10.2 K and 9.3 K respectively, with again generally less difference between the fire and non-fire pixels. These results demonstrate that potential active fire pixels located under optically thin cloud (as defined by the CT mask) often do not produce as strong a contrast with the background as do active fire pixels burning under clear sky conditions, resulting in the fire signal under optically thin cloud often being too weak for the FTA algorithm to detect. For this reason, no further attempt to

detect active fire pixels burning under cloud was made in the current LSA SAF processing chain.

Figure S2 in the Supplementary Materials shows an example of the final FRP-PIXEL Quality Product classification scheme, where fires are seen but where most pixels are cloudy and non-cloudy land pixels or 'not processed' water pixels (masked even prior to the cloud masking stage). To further minimize numbers of false active fire detections caused by unmasked cloud or water, the FTA algorithm originally masked certain pixels immediately neighbouring cloudy pixels or which are within two pixels of a 'not processed' water body pixel (masked as “Cloud/Water Edge” (Class 8; Table S1) if they fail to show a strong IR3.9 channel ( $BT_{3.9}$ ) signal:

$$BT_{3.9} < 320 \text{ K} \quad (4)$$

Whilst this test was designed to limit numbers of false fire detections, more recent testing indicated that the adjusted CMA mask is so effective at detecting cloud that the further cloud-edge test is unnecessary. Its removal successfully reduces errors of omission of active fires with respect to the MODIS active fire products by ~2% (FTA algorithm omission errors are around 70%; see Roberts *et al.*, 2015 for details). Similar testing for the water edge masking showed however that errors of commission increased by ~1% on its removal, and so the test was left in place despite it meaning that many fires burning immediately next to water bodies fail to be detected. Water edge pixels are class 11 in the Quality Product (Table S1).

### 3.3. Identification of Potential Fire Pixels (PFP's)

This part of the FTA algorithm (boxed in Figure 3) identifies all SEVIRI level 1.5 pixels that potentially could contain actively burning fires. First, two spectral thresholding tests related to the IR3.9 ( $BT_{3.9}$ ) and BTD ( $BT_{3.9} - BT_{10.8}$ ) signals must be passed, with thresholds varying with solar zenith angle ( $\theta_s$ ):

$$BT_{3.9} > C_{11}\theta_s + C_{12} \quad (5)$$

$$BT_{3.9} - BT_{10.8} > C_{21}\theta_s + C_{22} \quad (6)$$

where  $C_{11}$  (-0.3 and 0.0),  $C_{12}$  (310.5 K and 280 K),  $C_{21}$  (-0.0049 and 0.0) and  $C_{22}$  (1.75K and 1.0 K) are constants applied when  $\theta_s > 60^\circ$  and  $< 60^\circ$  respectively. The advantage of using these relatively low BT thresholds to discriminate any pixel conceivably containing an active fire is somewhat counteracted by fact that large areas of homogeneously sun warmed areas can often also exceed them, leading to significant and unwanted computational demands during subsequent processing stages. To avoid this, a series of standard high pass ‘edge detecting’ spatial filters of size  $3 \times 3$ ,  $5 \times 5$  and  $7 \times 7$  pixels are applied to the BTD ( $BT_{3.9} - BT_{10.8}$ ) image, and each PFP output from Tests (5) and (6) must pass the following two tests to remain as a PFP:

$$P = H_{filter} \geq DT \times \delta_{filter} \quad (7)$$

$$DT = 2.5 - 0.012 \times \theta_s \quad (8)$$

where  $H_{filter}$  is the output of the high pass spatial filter, and  $\delta_{filter}$  is a threshold that in the FTA prototype was taken as the standard deviation of the filtered BTM image. To further minimise computational demands during real-time processing, in the operational FTA algorithm  $\delta_{filter}$  was derived once for each filter size for each daily timeslot using four exemplar SEVIRI images, and the minimum  $\delta_{filter}$  for each timeslot and filter size used in Equation (7) during operational processing. The dynamic nature of this threshold is now being returned to the operational chain (Figure 3), since new testing has shown that use of the dynamic threshold reduces active fire detection errors of commission with respect to MODIS by 2% compared to the static case (see Roberts *et al.*, 2015).

### 3.4 Sunlint Detection

A sunlint angle ( $\theta_g$ ) is defined for each SEVIRI pixel according to Prins *et al.* (1998), and those pixels with  $\theta_g < 5^\circ$  are coded as glint-affected 'Class 4' in the FRP-PIXEL Quality Product (Table S1) and removed prior to the tests described in Section 3.3. Two further glint tests are applied after PFP identification, to discriminate more ambiguous glint using the ratio of the IR3.9 and VIS0.6 spectral radiances:

$$\frac{L_{3.9}}{L_{0.64}} < \frac{0.7}{p} \quad (9)$$

$$(2 - p) \cdot \frac{L_{3.9}}{L_{10.8}} < 0.0195 \quad (10)$$

where  $L_{3.9}$ ,  $L_{0.64}$  and  $L_{10.8}$  are the spectral radiance of the IR3.9, VIS0.6 and IR10.8 channels respectively, and  $p$  can take a value of either 1 or 2. We assume that the absence of nearby cloud makes it less likely that a particular PFP is caused by glint, so tests (9) and (10) work on the  $15 \times 15$  pixel window surrounding each PFP, and if this window contains a cloudy pixel then  $p$  is set to 1, otherwise to 2. Pixels satisfying these two tests are coded as 'possibly glint affected' (Class 5), whilst all processed pixels not belonging to the potential fire pixel (PFP) set and which have not yet received an alternative classification are coded as Class 0 ('not a potential fire pixel').

### 3.5 Contextual Active Fire Detection

During this Stage, an expanding 'background window' surrounding each PFP is used to calculate a set of metrics against which the PFP signal is compared, to confirm whether or not it should be classed as a presumed 'true' fire pixel. The window starts at  $5 \times 5$  pixels and expands until sufficient pixels meet the validity criteria outlined in Roberts and Wooster (2008); namely being cloud free, not a PFP, and passing the following tests which relate, respectively, to not showing the types of spectral

signature associated with a possible fire pixel (Tests 11 and 12), not being affected by remaining sunglint (Test 12), and having spectral signatures less like a fire than that of the PFP under test (Tests 14 and 15).

$$\frac{L_{3.9}}{L_{10.8}} < 0.0195 \quad (11)$$

$$BT_{3.9} - BT_{10.8} < 10 \text{ K} \quad (12)$$

$$\theta_g > 2^\circ \quad (13)$$

$$BT_{3.9} - BT_{10.8} < (BT_{3.9} - BT_{10.8})_{PFP} \quad (14)$$

$$BT_{3.9} < BT_{PFP_{3.9}} \quad (15)$$

Where the terms retain their already identified meanings, and  $BT_{D_{PFP}}$  and  $BT_{PFP_{3.9}}$  are, respectively, the BT difference of the potential fire pixel calculated using the IR3.9 and IR10.8 SEVIRI channels, and the PFPs IR3.9 channel BT.

When defining the operational FTA algorithm, we investigated the detailed characteristics of the aforementioned background window, aiming to elucidate the cause and consequences of certain SEVIRI imaging artefacts that impact the required statistics (e.g. the lowered IR3.9 brightness temperatures seen surrounding certain active fire pixels in Figure 6). To deliver the anti-aliased properties specified for SEVIRI level 1.5 imagery (Just, 2000; Deneke and Roebeling 2010), a Finite Impulse Response (FIR) digital filter is applied to each line of SEVIRI data, the filter consisting of a symmetric Sinc function having 17 coefficients (including some negative coefficients, Figure 7a), multiplied by a modified Kaiser window function. Such filtering can have particularly significant consequences in areas of high image contrast, and to investigate this we convolved the FIR filter with the SEVIRI point spread function (PSF) (Figure 7b) and applied the result to simulated thermal imagery containing active fires derived at a spatial resolution 10× higher than that of the native SEVIRI pixels. The convolution of the negative coefficients of the FIR filter and the strong IR3.9 channel active fires signals led to substantial decreases in the output IR3.9 channel brightness temperatures, both up- and down-scan of the fire pixel itself (Figure 6a), an effect mirroring that seen in real level 1.5 SEVIRI data (Figure 6b).

Further simulations, including of larger fires (e.g. Figure 7c and 7d), indicate that the orientation of the fire along or perpendicular to the SEVIRI scan line, and even the fires sub-pixel location, affects the final image details. Freeborn *et al.* (2014b) recently demonstrated how the sub-pixel fire location affects the MODIS-measured FRP, an effect previously identified with the BIRD HotSpot Recognition Sensor (Zhukov *et al.*, 2006). Calle *et al.* (2009) also reported related phenomena in SEVIRI data. Our simulations lead us to conclude that FIR-filter 'smearing' of the fire emitted spectral radiance into neighbouring pixels, and the depression of the IR3.9 BT of neighbouring pixels, can have significant consequences for active fire observations, particularly so if pixels now containing some of the fire emitted signal are not

themselves sufficiently strongly radiating to be detected as active fires (and/or if the background window statistics are unduly contaminated by lowered IR3.9 BTs).

Based on our simulations, we requested a period of Meteosat 'special operations', where near-simultaneous data from two MSG satellites could be compared with and without the FIR filter applied. These data are more fully described in Section 5.2, and confirm that decreased IR3.9 channel BTs are not seen neighbouring strongly radiating active fire pixels when Level 1.5 imagery is pre-processed without the FIR filter being applied (Figure 8). Further analysis confirms that when calculating the ambient background window statistics for a potential fire pixel (PFP), excluding the eight pixels immediately neighbouring the PFP improves the ambient background representation, since these are most affected by the FIR filtering (Figure 8). This exclusion is implemented in the operational FTA algorithm, as well as the requirement that when  $\theta_s > 70^\circ$  any further retained background window pixel must satisfy  $BT_{3.9} > 270\text{ K}$ .

The expanding background window starts at  $5 \times 5$  pixels, and expands by two in each direction until 65% of pixels are considered valid according to the aforementioned criteria (excluding the central  $3 \times 3$  pixels). For more than 95% of PFPs, a  $5 \times 5$  window is sufficient to meet this criteria, but expansion up to  $15 \times 15$  is allowed. In very rare cases where this is insufficient, the PFP is coded as having 'insufficient background pixels' for confirmation as an active fire ('Class 6') in the FRP-PIXEL Quality Product (Table S1). In all other cases, a series of statistical metrics derived from the correctly sized background window are used in a set of 'spatial contextual' tests to confirm whether the PFP can be classed as a 'true fire pixel'. These confirmatory tests are fully described in Roberts and Wooster (2008), and remain unaltered in the operational FTA algorithm and so are not detailed here. They rely on the assumption that the statistical average of the valid background window is representative of the signal the central 'PFP' would have had if it had not contained a fire, and this was examined by selecting random non-fire level 1 pixels and re-classifying them as PFPs such that their signals could be compared to those of their background windows (Figure 9). Apart from GLC2000 pixels classed as 'swamp', for 80% of cases examined the mean IR3.9 channel BT of the background window was within 1 K of the central 'PFP' pixel  $BT_{3.9}$ , and always within 2 K. 'Swamp' forms a very small fraction of the SEVIRI disk, and differences here increased up to 6 K, presumably due to spatially varying percentage covers of water and land. Furthermore, in all cases the standard deviation of the background window IR3.9 channel spectral radiance was always larger than the actual difference between that of the central pixel and the window mean, and since the former provides a measure of the background window characterisation random error for use during FRP uncertainty specification (Section 5.1), this indicates the conservative nature of the resulting uncertainty estimate.

Based on the results of the background window spatial contextual tests, PFPs classed as 'true fire pixels' are coded as Class 1 in the Quality Product (Table S1), and have



their FRP derived (Section 5). For confirmed fire pixels with a saturated IR3.9 channel signal ( $BT_{3.9} \geq 335 \text{ K}$ ), FRP is still estimated but with adjustments for channel saturation (Section 5.2.1) and the pixel is coded as Class 2. PFPs failing the spatial contextual tests altogether are coded as Class 7 (Table S1). After this each confirmed fire pixel is given a detection confidence measure (0 to 1), based on the approach of Giglio *et al.* (2003) as described in Roberts and Wooster (2008).

## 4. FRP DERIVATION

### 4.1 Derivation of Per-Pixel FRP Values

All confirmed active fire pixels (Classes 1 and 2 in the FRP-PIXEL Quality Product) have their FRP estimated using the MWIR radiance method of Wooster *et al.* (2003; 2005). This requires quantification of the fires' contribution to the active fire pixels elevated IR3.9 channel signal, and bases this on the difference between the fire pixels' IR3.9 channel spectral radiance ( $L_f$ ) and the mean spectral radiance ( $L_b$ ) of the surrounding background window:

$$FRP = \frac{\pi \sigma A_n}{\tau_{MWIR} C_a \cos(\theta_v)} (L_f - L_b) \quad (16)$$

where  $L_f$  and  $L_b$  are expressed in  $\text{mW} \cdot \text{m}^{-2} \cdot \text{sr}^{-1} \cdot (\text{cm}^{-1})^{-1}$ ,  $\tau_{MWIR}$  is the atmospheric transmittance calculated for the SEVIRI IR3.9 channel,  $C_a$  ( $\text{mW} \cdot \text{m}^{-2} \cdot \text{sr}^{-1} \cdot (\text{cm}^{-1})^{-1} \cdot \text{K}^{-4}$ ) is a constant determined according to Wooster *et al.* (2003; 2005),  $\theta_v$  is the view zenith angle ( $^\circ$ ) and  $A_n$  is the SEVIRI ground pixel area at the sub-satellite point ( $\text{km}^2$ )

### 4.2 Method for FRP Atmospheric Correction

Wooster *et al.* (2005) demonstrate that the primary atmospheric effect with regard to FRP derivation is the non-unitary MWIR atmospheric transmission ( $\tau_{MWIR}$ ), and that upwelling atmospheric path radiance and reflected downwelling atmospheric radiance are able to be neglected due to the fire pixel and immediately surrounding background area radiances are differenced in Equation 16. However, the specification of  $\tau_{MWIR}$  is complicated by the fact that the transmittance and fire-emitted spectral radiance signals are far from uniform across the SEVIRI's IR3.9 spectral bandpass. Figure 10 shows the IR3.9 band spectral response function along with the transmittance of the US standard atmosphere. The impact of the strong  $\text{CO}_2$  absorption band on overall atmospheric transmission upwards of  $\sim 4.0 \mu\text{m}$  can be clearly seen, and SEVIRI's IR3.9 band remains sensitive to MWIR radiation at wavelengths longer than  $4.2 \mu\text{m}$ , though in fact no surface-emitted radiance reaches the sensor directly at these wavelengths. Many other atmospheric absorption features are seen across the bandpass, many of which depend on the atmospheric total column water vapour (TCWV) content. Also plotted on the right hand side y-axis of Figure 10 is the bottom of atmosphere (BOA) spectral radiance emitted by a 310 K blackbody, along with the

equivalent top of atmosphere (TOA) measure calculated using MODTRAN 5 (Berk *et al.*, 2005).

When selecting the appropriate atmospheric transmittance to derive a band-integrated TOA radiance signal from a BOA measure, it is quite common to use a band-averaged  $\tau_{MWIR}$  (e.g. Qin and Karnieli, 1999). However, as can be seen in Figure 10, this not fully appropriate with regard to SEVIRI's IR3.9 band, across which the atmospheric transmittance and ground (and fire) emitted spectral radiance vary significantly. Specifically, across SEVIRI's IR3.9 band, atmospheric transmittance generally decreases with increasing wavelength, whereas upwelling spectral radiance generally increases. Converting the band-integrated TOA spectral radiance to a BOA measure simply using the mean  $\tau_{MWIR}$  calculated across the IR3.9 spectral bandpass would therefore increase the contribution of the shorter wavelength TOA signal to the band-integrated BOA spectral radiance too much, and the longer wavelength signal too little. This effect is more significant here than for narrowband channels such as the MODIS 3.95  $\mu\text{m}$  Band 21, because SEVIRI's IR3.9 band has significant sensitivity around the 4.2  $\mu\text{m}$   $\text{CO}_2$  absorption region where MWIR atmospheric transmittance is at its lowest but the surface emitted signal is at its highest. Using a band-averaged  $\tau_{MWIR}$  to convert the TOA radiance simulated in Figure 10 to a BOA signal results in a latter estimate almost 10% too low, even when the band-averaged transmittance includes consideration of the spectral response function weighting.

In simulations such as those shown in Figure 10, the spectral shape of the surface emitted signal and the atmospheric transmittance spectrum are known, and can be used to apply the correct transmittance at each observation wavelength. However, true SEVIRI IR3.9 observations do not resolve the incoming signals spectral behaviour. Therefore, the  $\tau_{MWIR}$  to include in Equation 16 is best calculated as an effective (or 'pseudo') atmospheric transmittance, determined from pre-computed radiative transfer simulations of top-of-atmosphere (TOA) and bottom-of-atmosphere (BOA) fire pixel and background pixel spectral radiance difference signals:

$$\tau_{MWIR} = \frac{\int_3^5 \widetilde{B}(T_f)^{TOA} - \int_3^5 \widetilde{B}(T_b)^{TOA}}{\int_3^5 \widetilde{B}(T_f)^{BOA} - \int_3^5 \widetilde{B}(T_b)^{BOA}} \quad (17)$$

where  $\int_3^5 \widetilde{B}(T)$  indicates the spectral radiance calculated using the Planck function at brightness temperature  $T$  (Kelvin), convolved with the spectral bandpass of the SEVIRI IR3.9 band and integrated over the 3-5  $\mu\text{m}$  spectral range, the subscripts  $f$  and  $b$  correspond to the fire pixel and the background windows respectively, and the superscripts BOA and TOA indicate the bottom- and top-of-atmosphere measures.

For the operational LSA SAF processing chain generating the FRP-PIXEL products, Equation (17) was used to generate a look-up-table (LUT) of  $\tau_{MWIR}$  using the RTMOM and latterly the MODTRAN5 atmospheric radiative transfer models (Govaerts 2006 and Berk *et al.* 2005 respectively) with varying total column

atmospheric water vapour (TCWV) content ( $U_{H2O}$ ; varying between 0.5 and 60 kg.m<sup>-2</sup>), view zenith angle ( $\theta_v$ ), a range of standard atmospheres (tropical, mid-latitude summer, etc), fire pixel ( $T_f$ ) and background pixel ( $T_b$ ) pixel integrated brightness temperatures (300 - 330 K and 290 - 320 K respectively), aerosol optical thicknesses, and atmospheric CO<sub>2</sub> and ozone column amounts. At the latitude/longitude location and view zenith angle ( $\theta_v$ ) of each confirmed active fire pixel identified by the FRP-PIXEL processing chain,  $\tau_{MWIR}$  is retrieved from this LUT based on the TCWV content taken from ECMWF short-term forecasts available at 0.5° spatial resolution every 3 hrs. As an example, at the sub-satellite point ( $\theta_v = 0$ ) for a typical  $U_{H2O}$  of 20 kg m<sup>-2</sup> and a mid-latitude summer atmosphere, Equation (17) indicates  $\tau_{MWIR}$  as 0.69 for use in Equation (16), compared to 0.74 for the IR3.9 band-averaged value. During this process, the uncertainty in the effective  $\tau_{MWIR}$  ( $\sigma_\tau$ ) is also specified for use in the uncertainty calculations described in Section 5.

## 5. FRP UNCERTAINTY CALCULATIONS AND THE MSG 'SPECIAL OPERATIONS MODE' OBSERVATION PERIOD

### 5.1 FRP Uncertainty Formulation

A full per-pixel FRP uncertainty ( $\sigma_{FRP}$ , MW) is specified at each detected active fire pixel in the FRP-PIXEL product, derived by combining the absolute uncertainties ( $\sigma_{V_k}$ ) of the four variables ( $C_a$ ,  $\tau_{MWIR}$ ,  $L_f$  and  $L_b$ ) of Equation 16:

$$\sigma_{FRP} = FRP \sqrt{\sum_{k=1}^4 \sigma_{V_k}^2 \left( \frac{\partial FRP}{\partial V_k} \right)^2} \quad (18)$$

where  $V_k$  represents the variables of Equation 16 ( $C_a$ ,  $\tau_{MWIR}$ ,  $L_f$  and  $L_b$  respectively) and where the absolute uncertainties ( $\sigma_{V_k}$ ) in these are assumed uncorrelated. Solving for the partial derivatives in Equation (18) gives:

$$\sigma_{FRP} = FRP \left[ \left( \frac{\sigma_{C_a}}{C_a} \right)^2 + \left( \frac{\sigma_{\tau_{MWIR}}}{\tau_{MWIR}} \right)^2 + \left( \frac{\sigma_{L_b}}{L_f - L_b} \right)^2 + \left( \frac{\sigma_{L_f}}{L_f - L_b} \right)^2 \right]^{1/2} \quad (19)$$

where each term takes the following values:

$\sigma_{C_a}$  is the variability in the  $C_a$  'FRP coefficient' (mW.m<sup>-2</sup>.sr<sup>-1</sup>.(cm<sup>-1</sup>)<sup>-1</sup>.K<sup>-4</sup>) used in Equation 16, which across the specified active fire temperature range of 650 - 1350 K equates to a  $\left( \sigma_{C_a} / C_a \right)$  value of ~ 10% (Wooster *et al.*, 2005).

$\sigma_{\tau_{MWIR}}$  is the variability in calculated atmospheric transmissivity, specified in Section 4.2 and resulting from uncertainties in the TCWV and in other atmospheric parameters used in the radiative transfer modelling.

$\sigma_{L_b}$  is the standard deviation of the background window pixels spectral radiance ( $\text{mW.m}^{-2}.\text{sr}^{-1}.\text{(cm}^{-1})^{-1}$ ), calculated as discussed in Section 3.5 and adjusted for the atmospheric pseudo transmittance ( $\tau_{MWIR}$ ).

$\sigma_{L_f}$  is the uncertainty in the measured fire pixel spectral radiance ( $\text{mW.m}^{-2}.\text{sr}^{-1}.\text{(cm}^{-1})^{-1}$ ) resulting from a combination of (i) the SEVIRI sensors radiometric noise ( $\sigma_L$ ), (ii) instances of IR3.9 band sensor saturation ( $\sigma_S$ ), and (iii) influences from the pre-processing steps used to generate the SEVIRI level 1.5 data from the raw observations (termed here  $\varepsilon_p$ ), for example the application of the FIR filter detailed in Section 3.5. These three contributions are represented by the three fractional terms of Equation (20), where  $L_f$  remains as the measured radiance of the active fire pixel ( $\text{mW.m}^{-2}.\text{sr}^{-1}.\text{(cm}^{-1})^{-1}$ ) and  $S$  is its estimated adjusted radiance in the case of IR3.9 channel saturation (see Section 5.2.1 for specification of  $S$  and  $\sigma_S$ ):

$$\sigma_{L_f} = L_f \sqrt{\left[\left(\frac{\sigma_L}{L_f}\right)^2 + \left(\frac{\sigma_S}{S}\right)^2 + \varepsilon_p^2\right]} \quad (20)$$

The “end of life” radiometric noise prediction of the SEVIRI IR3.9 channel is 0.17 K (Schmetz *et al.* 2002; Hewison and Muller 2013), translating to  $\sigma_L = 0.038 \text{ mW/m}^2/\text{sr/cm}^{-1}$  ( $0.025 \text{ W/m}^2/\text{sr}/\mu\text{m}$ ). To specify the remaining terms, a series of unique Meteosat-8 SEVIRI observations were made.

## 5.2 Meteosat-8 Special Operations Mode: Data Collection and Analysis

Between 3<sup>rd</sup> – 7<sup>th</sup> September 2007, Meteosat 8 was operated in 'rapid scan' mode, imaging every four minutes between 3° N and 33° S, with a cycle of additional adjustments:

- i) 'Low gain' operation of the IR3.9 channel, allowing measurements to 375 K.
- ii) Alteration of the Meteosat Main Detection Unit (MDU) standard SEVIRI Finite Impulse Response (FIR) filter ( Figure 7) to a 1 pixel wide rectangular ‘top-hat’ function that allows the original observations to be transmitted to the Primary Ground Station for use in level 1.5 generation.

The Meteosat-8 'Special Operations' period was aimed at both assessing the individual uncertainty terms in Equation (20), and their aggregate effect. Near-simultaneous observations from the normally operating Meteosat-9 were acquired for comparison.

### 5.2.1 Effect of IR3.9 Band Saturation

SEVIRI saturates at a DN of 1023, equating to an IR3.9 channel brightness temperature ( $BT_{3.9}$ ) of just over 335 K ( $\sim 3.6 \text{ mW m}^{-2} \text{ sr}^{-1} (\text{cm}^{-1})^{-1}$ ) in standard operating mode. Roberts and Wooster (2008) reported that IR3.9 saturation normally occurs in no more than a few percent of level 1.5 active fire pixels, coded as Class 2 in the FRP-PIXEL Quality Product (Table S1). Although such pixels share the same  $BT_{3.9}$ , application of Equation (16) would not necessarily give them the same FRP, since this depends also on the background window radiance, pixel area (and thus view zenith angle;  $\theta_v$ ) and  $\tau_{MWIR}$ . Around the SSP, IR3.9 saturation occasionally occurs at FRPs as low as 45 MW, if the fire is burning upon a particularly warm daytime background ( $\geq 330 \text{ K}$ ), but more typically at  $\sim 250 \text{ MW}$ . Further from the SSP, FRPs more than double this can be measured without saturation. Our primary aim was to determine which FRP ( $S$ ) to record at saturated IR3.9 pixels, and with what uncertainty ( $\sigma_S$ ), which is used in Equation 20. Barnie *et al.* (2015) tackled a similar problem with respect to volcanic thermal features.

We first explored the impact of the level 1.0 to level 1.5 IMPF conversion procedures, which involve geometrically resampling data using a bi-cubic function. We found IR3.9 saturation to be more prevalent in the level 1.0 data, as the resampling has the effect of smearing some fire pixel signals from saturated to unsaturated (Figure 11). We used the Meteosat-8 'special operations' data that included a low-gain IR3.9 operation (Table 2) to quantify the impact further. When the IMPF used a nearest neighbour geometric resampling scheme, rather than the standard resampling scheme, the resulting level 1.5 data showed not a single saturation event, with the highest IR3.9 signal being  $6.7 \text{ mW m}^{-2} \text{ sr}^{-1} (\text{cm}^{-1})^{-1}$  (373 K) and an FRP of 1989 MW (Equation 16 at  $\theta_v$  of  $14^\circ$ ). Figure 12a shows the frequency distribution of per-pixel FRP recorded at active fire pixels detected in level 1.5 data that would normally have been saturated under standard SEVIRI operations. Artificially capping the IR3.9 brightness temperatures of these pixels at the standard 335 K saturation temperature and recalculating their FRP using Equation (16) allowed for a FRP comparison of these 'simulated saturated' data to that from the unsaturated (low-gain) observations. Not unexpectedly, the greatest impact of IR3.9 band saturation occurs near the peak of the typical fire diurnal cycle seen in Figure 2, when around 5% of the level 1.5 pixels would have been saturated under 'standard' operations and where total southern African FRP would consequently be underestimated by around 13%. At night these values alter to a maximum of 4% and 5% respectively, and since regional FRP at night is typically very low (Figure 2) the absolute amount of FRP underestimation at night is rather negligible. The data shown in Figure 12, along with the equivalent derived from our 'simulated saturated' data, were used to provide the replacement IR3.9 band spectral radiance for saturated pixels (specified as  $S$  and the associated uncertainty  $\sigma_S$  in Equation 20) that are coded as 2 in the Quality Product (Table S1), which was also used to replace  $L_f$  in Equation 16.  $S$  and  $\sigma_S$  were based on the median ( $4.08 \text{ mW m}^{-2} \text{ sr}^{-1} (\text{cm}^{-1})^{-1}$ ) and median absolute deviation from the median ( $0.49 \text{ mW m}^{-2} \text{ sr}^{-1} (\text{cm}^{-1})^{-1}$ ) of the IR3.9 spectral radiances of Figure 12, rather than the mean

and standard deviation, due to the non-normal distribution. Figure 12b shows the resulting data, stratified by  $\theta_v$  (intervals  $25^\circ$  to  $30^\circ$  and  $30^\circ$  to  $35^\circ$  contain the vast bulk (79%) of the data). Since pixel area and atmospheric transmittance increase with  $\theta_v$ , the FRP of pixels that would saturate under standard operating conditions generally increases with view zenith angle ( $\theta_v$ ). For each fire pixel, which would normally have been saturated, replacing their actual spectral radiance with  $S$  and specifying the uncertainty  $\sigma_S$  gives a 'predicted' median FRP for each  $\theta_v$  interval that is a reasonable fit to the observed distribution calculated using the unsaturated IR3.9 observations made during the 'special operations' period. Thus, under normal operations, the use of this saturation adjustment provides an estimate of FRP closer to the real emitted FRP than would be the case if the pixels saturated radiance measures had been maintained.

### 5.2.2 Impact of SEVIRI Level 1.0 to 1.5 Conversion

Raw SEVIRI data undergoes prior to its conversion to level 1.5 (Section 2.2). To assess the impacts of the SEVIRI pre-processing (Section 2.20) we again used Meteosat-8 “Special Operations” data, specifically that when the onboard and on-ground processing chain of SEVIRI was altered to replace the standard FIR filter with the top-hat rectangular filter of single pixel width, and where the level 1.5 data were delivered using both bi-cubic and nearest neighbour geometric resampling schemes. Meteosat-8 and -9 level 1.5 “Standard Mode” data full disk data intercomparisons were undertaken first to elucidate initial differences between the two sensors. Using simultaneous observations of over 35,000 active fire pixels, Meteosat-8 was found to measure IR3.9 spectral radiances on average  $1.0 \pm 7.7\%$  (mean  $\pm$  standard deviation) lower than Meteosat-9 (Figure 13), with the bias most likely the results of Meteosat-9 at the time being positioned  $3.4^\circ$  further West than Meteosat-8 and thus with a different view zenith angle and ground pixel area. The variability likely stems from different sub-pixel positions of the fires, whose impact was illustrated in Freeborn *et al.* (2014c) for MODIS. The degree of difference altered as the 'special operations' rapid-scan Meteosat-8 data were substituted, with observations now being made approximately 1 minute apart due to the different scanning schemes used on the two satellites. From these data, the separate uncertainty coming from the measurement time-differences and the differing data processing chains were calculated, and the uncertainty impact of the level 1.0 to level 1.5 processing operations ( $\epsilon_p$ ) was estimated as 0.084 (8.4%) for use in Equation 20.

For illustration of the impact that different SEVIRI pre-processing operations can have on the active fire data, Figure 14 includes 'total scene' FRP comparisons of Meteosat-8 data processed using the standard FIR (Sinc) and top-hat filters, and nearest neighbour and bi-cubic geometric resampling schemes. The top hat filter allows lower FRP active fire pixels to be detected, giving a lower minimum total scene FRP than is obtained when applying the standard FIR-filter (which tends to 'smear' fire pixel radiances). The geometric resampling scheme used also impacts total

scene FRP to a greater extent when the FIR filter is applied, with larger impacts for scenes containing only a relatively few lower FRP active fire pixels (upon whose detectability the filter selection will impact most strongly). Further investigation shows that the radiometric uncertainty of the active fire pixel radiance is the largest contributor to the overall FRP uncertainty defined by Equation 19, and that consideration should be given to optimising SEVIRI level 1.0 to level 1.5 pre-processing operations with respect to active fire data in order to minimise this.

## 6. LSA SAF SEVIRI FRP-GRID PRODUCT

### 6.1. Product Justification, Derivation, and Implementation

Whilst Section 5 shows that some optimisation of the IMPF level 1.5 data pre-processing chain could still be made for the active fire application, when viewing the same ground area at the same time (as occurs a few times per day), MODIS (with a higher spatial resolution and higher MWIR band saturation limit) will generally offer a better opportunity to detect the true regional-scale FRP of landscape-scale fires than SEVIRI. A comparison of the frequency-magnitude distribution of concurrent and collocated SEVIRI and MODIS FRP observations indicates the notable biases of SEVIRI (Figure 15). SEVIRI's statistical distribution of measured per-pixel FRP ( $\mathcal{H}$ ) is right skewed, and can be divided into three broad regimes. Between  $\mathcal{H}_L$  and  $\mathcal{H}_U$ , the distribution follows a power-law, with SEVIRI detecting fewer active fire pixels with increasing FRP owing to the true rarity of extreme (high FRP) fire behaviour on the landscape. In the lower regime (below  $\sim 30 - 40$  MW),  $\mathcal{H}$  deviates from this power-law as the performance of the FTA algorithm applied to SEVIRI is increasingly limited by the fact that low FRP fires are increasingly difficult to distinguish above the ambient background variability, and many thus remain undetected. Roberts *et al.* (2015) provide a full assessment of this effect using scene-to-scene comparisons between SEVIRI FRP-PIXEL products and MODIS active fire data. Finally, above  $\mathcal{H}_U$  SEVIRI's per-pixel FRP distribution suffers from right hand truncation due to IR3.9 band saturation, albeit in the final FRP-PIXEL product this is adjusted for using the methods detailed in Section 5.2.1.

The above issues lead to a general underestimation of regional-scale FRP totals measured by SEVIRI when compared to simultaneously recorded MODIS data (Roberts and Wooster, 2008; Roberts *et al.*, 2015). Providing adjustment for this, and for varying levels of cloud cover, whilst maintaining a temporal resolution still significantly higher than that offered by polar orbiting systems, is the role of the SEVIRI Level 3 FRP-GRID Product. The product combines information contained within all FRP-PIXEL files collected each hour, and delivers a cloud-cover and bias-adjusted, spatio-temporal full-disk summary product at a  $5^\circ$ /hourly resolution (Figure 16).

Freeborn *et al.* (2009) indicated that, in general, when viewing African areas simultaneously, MODIS measures on average around twice the FRP measured by



SEVIRI. However, large regional and temporal differences exist, and Freeborn *et al.* (2014a) recently demonstrated that over smaller 1° areas within a single country (in this case the Central African Republic, one of the most fire-affected African countries) SEVIRI's active fire error of omission with respect to MODIS varies between 25% and 74% (depending on the locations fire regime), causing a similar variation in the degree of FRP underestimation. It is clear from such analysis that spatially varying bias-adjustment factors are required in the FRP-GRID product, and these were derived using a set of coincident SEVIRI and MODIS active fire observations (May 2008 - May 2009), with both datasets atmospherically corrected using the Section 4.2 scheme. SEVIRI active fire pixels were accumulated over one hour, and to achieve a sufficient active fire pixel sample size, matching MODIS and SEVIRI active fire detections were accumulated within 5° grid cells. To minimize MODIS edge-of-scan effects (Freeborn *et al.*, 2009; 2011; 2014b) only MODIS data within the centre two thirds of the swath were used. Half the resulting data were used as the training dataset, and half for the performance evaluation reported in Roberts *et al.* (2015). Figure 17 illustrates the methodology, with the summed atmospherically corrected FRP measured by MODIS within each 5° grid cell ( $\sum FRP_G$ ) related to that measured by SEVIRI using:

$$\sum FRP_G = \alpha_{ROI} \left( \frac{1}{n} \sum_{t=1}^n \sum FRP_{SEVIRI,t} \right)^{\beta_{ROI}} \quad (22)$$

where the value in parenthesis on the right hand side represents the atmospherically corrected sum of FRP measured by SEVIRI in the 5° cells averaged over the  $n$  preceding timeslots available in one hour (where  $n = 4$ , typically) and the factors  $\alpha$  and  $\beta$  are power law parameters. The spatial variation was considered by calculating these factors separately for each of the four LSA SAF geographic regions. Equation 22 therefore converts aggregate SEVIRI-derived FRP measures into that which would have been measured by MODIS when viewing the area within the centre 2/3<sup>rd</sup>s of its swath. The exponent  $\beta$  was functionally intended to allow for the fact that SEVIRI-to-MODIS ratios of FRP are generally lower during periods of reduced fire activity (Freeborn *et al.*, 2014a), but predictive abilities of this formulation proved to be no more skilful than a linear formulation so  $\beta$  was fixed at 1.0 and  $\alpha$  derived using a weighted least squares linear best fit to the median values of the training dataset (Figure 17). Final values of  $\alpha$  (and standard error) used in the FRP-GRID product are 1.674 (0.062), 1.464 (0.065), 2.057 (0.224) and 1.674 (0.173) for Nafr, Safr, Same and Euro respectively, and since the value for the European LSA SAF region was found statistically insignificantly different from that of North Africa it was assigned the same value since many more fires were available in North Africa to enhance relationship robustness.

Uncertainty ( $\sigma_G$ ) on the derived gridded FRP is specified as:



$$\sigma_G = \sqrt{\sum_{k=1}^2 \left( \frac{\partial G}{\partial V_k} \right)^2 \sigma_{V_k}^2} \quad (23)$$

where  $V_k$  represents the variables of Equation 22 contributing to the uncertainty in  $G$ , namely the coefficient  $\alpha$  and the mean FRP measured by SEVIRI in the grid cell over a one hour summation period. Expanding this expression:

$$\sigma_G = G \sqrt{\left( \frac{\sigma_{\alpha_{ROI}}}{\alpha_{ROI}} \right)^2 + \left( \frac{\sqrt{\sum_{i=1}^p \sigma_{FRP,i}^2}}{\sum_{t=1}^n FRP_{SEVIRI,t}} \right)^2} \quad (24)$$

where  $\sigma_{\alpha_{ROI}}$  is the uncertainty in  $\alpha$ ,  $p$  is the number of active fire pixels detected by SEVIRI in the grid cell during the hour, and  $\sigma_{FRP,i}$  is the uncertainty associated with the individual active fire pixel  $i$  given by Equation 19 and stored in the FRP-PIXEL product.

The FRP-GRID algorithm also bias adjusts the hourly averaged FRP by normalising by the hourly-averaged cloud cover fraction. This procedure is similar to that performed for MODIS by Giglio *et al.* (2006) and in Global Fire Assimilation System (GFAS) of the Copernicus Atmosphere Monitoring Service (Kaiser *et al.*, 2012). It is important to stress that the bias and cloud-cover adjustment procedures implemented during FRP-GRID processing are purely statistical in nature, and aimed at reducing the impact of regional scale biases occurring when data are accumulated over multiple time-slots. Importantly, the cumulative FRP detected by the original FRP-PIXEL products is obtainable from the FRP-GRID product, so that the user can remove, adjust, or apply their own bias corrections should they prefer. The datasets stored in the FRP-GRID files are shown in Table S2 in the Supplementary Materials, but many users may wish simply to focus on use of the FRP-PIXEL product itself.

## 8. PRODUCT COMPARISON AND TREND ANALYSIS

### 8.1 Comparison to other SEVIRI Active Fire Products

Since Roberts *et al.* (2005) published the first Meteosat SEVIRI active fire detection algorithm, other active fire studies have made use of SEVIRI data (e.g. Calle *et al.*, 2006; Amraoui *et al.*, 2010; Roberts and Wooster, 2014), some of which have resulted in routinely generated datasets (e.g. Carvalheiro *et al.*, 2010; Calle *et al.*, 2011). Roberts *et al.* (2015) report a detailed performance comparison and evaluation of many of these products compared to FRP-PIXEL, and Figure 18 demonstrates the magnitude of the differences that can occur, here between the WF-ABBA and FRP-

PIXEL products derived from the same level 1.5 data. Since we know that the FRP-PIXEL product undercounts active fire pixels below the  $\mathcal{H}_L$  threshold of Figure 15, we show both the total FRP-PIXEL fire pixel count at each timeslot, and that from pixels with FRP > 40 MW and > 50 MW. For many imaging slots, the FRP-PIXEL product detects around twice as many active fire pixels as does WF-ABBA, even when using the 'all detections' (unfiltered) WF-ABBA data. The latter appear also to show some potentially unrealistic temporal patterns, for example in (b) during the early morning of 31<sup>st</sup> Aug 2014 a local peak in fire pixel count is present at 7:00am local time and is quite possibly caused by glint effects. This local peak is reduced and finally removed by the more stringent WF-ABBA filtering, though this filtering also lowers the number of overall fire pixels recorded. Roberts *et al.* (2015) includes a much more complete active fire product intercomparison and performance evaluation, but the limited comparison provided here serves to indicate both the highly sensitive nature of the FTA algorithm, and its ability to screen out early morning sunglint induced false alarms without recourse to temporal filtering. Since fires in African landscapes quite often show up in a given pixel only once in a 24 hour period (either having moved into a neighbouring pixel as the fire spreads across the landscape, or being detected only occasionally due to the low FRP nature of the fire itself), the ability to perform sensitive and accurate active fire detection without having to filter out fire pixels detected only once during the day offers a useful capability.

## 8.2 Comparison to MODIS and Analysis of Active Fire Trends

The LSA SAF Meteosat SEVIRI FRP products are available since 2008, and in 2015/2016 a reprocessing is planned that will generate over a decade of data. Baldassarre *et al.* (2015) and Roberts *et al.* (2015) show how these products can be used to support fuel consumption rate estimation for use in high temporal resolution atmospheric modelling of smoke plume dispersion, whilst Freeborn *et al.* (2014a, c) demonstrate both their complementarity to MODIS and their ability to discriminate trends in fire behaviour. Figure 19 builds on this to show (a) MODIS MOD14/MYD14 and (b, c) SEVIRI FRP-PIXEL active fire detections collected over Central African Republic. The nearest temporally coincident SEVIRI active fire pixel for each MODIS active fire pixel was calculated based on the ground distance  $\Delta d$  between the pixel centres. Results indicate that 30%, 42%, and 53% of the MODIS active fire pixels had a SEVIRI counterpart detected at the same time (i.e. those in Figure 19b) and located within 3, 4, and 5 km, respectively, and only 10% had the spatially closest, simultaneously detected SEVIRI fire pixel located more than 20 km away. The same proximity analysis was repeated to include the full set of SEVIRI active fire pixels detected at all timeslots (i.e. all those mapped in Figure 19c), where 83%, 91%, and 95% respectively of MODIS fire pixels were found to have a SEVIRI fire pixel within 3, 4, and 5 km respectively and fewer than 1% did not have a SEVIRI counterpart within 20 km. The reverse analysis showed that almost every SEVIRI fire pixel had a MODIS fire pixel within 4 km of it (detected anytime within the two weeks). We conclude that, although the FRP-PIXEL product fails to detect a significant proportion of the MODIS active fire pixels at the time of

the MODIS overpass (Figure 19b), due to their FRP being below the  $\mathcal{H}_L$  threshold of Figure 15, the SEVIRI FTA algorithm does detect the vast majority of MODIS-detected fires at some earlier or later stage of their lifecycle (Figure 19c).

Figure 20 indicates the temporal cycle of SEVIRI active fire detections over the region shown in Figure 19, and the time difference within which the matching SEVIRI and MODIS detections of the same fire generally occur (with the matched detections taken as the SEVIRI detection with the minimum time difference to the MODIS detection and located within 4 km of it). Overall, 70%, 79%, and 84% of the collocated MODIS fire pixels were detected by SEVIRI within 12, 24 and 36 hrs respectively of the best matched MODIS observation, with the SEVIRI detection more commonly being after the MODIS detection, but quite often occurring before. The 15-minute repeat cycle of SEVIRI is well suited for capturing temporal fluctuations in fire behaviour (Roberts *et al.*, 2009a), and is able to capitalize on those opportune moments when a fire does become detectable, notwithstanding the relatively coarse pixel sizes available from geostationary orbit. Figure 21 shows a six year time-series over the same area with clear cyclic patterns and extremely low FRP pixels dominating outside of the main periods of fire activity. Biomass burning is spatially extensively in the CAR (Figure 19; Eva and Lambin, 1998; Bucini and Lambin, 2002; Freeborn *et al.*, 2014a, 2014c), and Figure 21 shows similar patterns in active fire pixel count and total FRP and with some suggestion of a generally decreasing trend in fire activity in recent years (as already noted by Freeborn *et al.* (2014c) using MODIS).

In terms of the FRP-PIXEL products ability to provide information relevant to individual large fire events, Figure 22 shows an example of high FRP ( $\geq 200$  MW per pixel) wildfires detected across the Mediterranean in July 2009 (Pausas and Fernández-Muñoz, 2012). Selecting the single fire pixel that corresponds to the intense wildfire that burned close to Sierra Cabrera (SE Spain), the timeseries shows that on 14<sup>th</sup> July this fire expanded and was burning fuel at a rate of 221 kg sec<sup>-1</sup> (calculated using the conversion factor of Wooster *et al.* (2005)) before dying out on the 15<sup>th</sup> July, matching well with news reports of the time ([http://en.wikipedia.org/wiki/2009\\_Mediterranean\\_wildfires](http://en.wikipedia.org/wiki/2009_Mediterranean_wildfires)). The same reports indicate that on 23<sup>rd</sup> July the fire flared again, and this second event is also observed in the FRP-PIXEL product time-series, with the FRP reaching similar heights as seen in the initial blaze (Figure 21c). FRE-estimated total fuel consumption is estimated to have been in excess of 11 thousand tonnes.

## 9. SUMMARY AND CONCLUSION

Satellite-based estimates of FRP, including from geostationary satellites, are increasingly used to support regional and global biomass burning emissions calculations (Remy and Kaiser 2014; Roberts *et al.* 2011; Vermote *et al.* 2009; Zhang *et al.* 2012; Turquety *et al.*, 2014; Baldassarre *et al.*, 2015). We have provided a

detailed description of the algorithms and information content of the operational SEVIRI FRP products available from the EUMETSAT Land Surface Analysis Satellite Applications Facility (LSA SAF), both the FRP-PIXEL product (3 km spatial resolution, every 15 mins), and the spatio-temporal summary FRP-GRID product that includes bias adjustments for cloud cover and SEVIRI's inability to detect the lowest FRP fire pixels. Further information on data formats and content are included in the Supplementary information.

Using the operational geostationary Fire Thermal Anomaly (FTA) algorithm described herein, SEVIRI detects active fire pixels with an FRP down to around 20 MW, but those with  $FRP < \sim 30\text{--}40$  MW are typically undercounted, hence the requirement for the bias-adjustment factors included in the FRP-GRID product. Using scene simulations and analysis of Meteosat-8 'special operations' data we demonstrate that certain of the data pre-processing procedures applied onboard the MSG satellites or in the EUMETSAT Image Processing Facility (IMPF), maybe non optimum for the active fire application. Standard cloud masking procedures also need to be optimised, since they can otherwise mask smoke, or even active fires, as cloud. We recommend consideration of these issues when designing the pre-processing and cloud masking chains to be used with Meteosat Third Generation (MTG), whose sensor has a dedicated low gain MWIR channel to support active fire applications (Just *et al.*, 2014). Comparisons to the WF-ABBA SEVIRI product indicates strong performance of the FTA algorithm, which detects substantially more active fire pixels, both in any particular SEVIRI timeslot and over the full diurnal cycle. The LSA SAF FRP products are therefore well suited to prescribing the typical diurnal cycle of biomass burning regions (Turquety *et al.*, 2014; Andela *et al.*, 2015), and for estimating high temporal resolution wildfire smoke emissions for atmospheric modelling (Baldassarre *et al.*, 2015; Roberts *et al.*, 2015).

## Acknowledgements

Thanks to G. Fowler and other EUMETSAT staff who contributed to discussions and to our ability to conduct the Meteosat-8 Special Operations. We also thank Isabel Trigo and all LSA SAF staff for their continued support and dedication. We acknowledge the team that provide the WFABBA products, which were developed at the Cooperative Institute for Meteorological Satellite Studies (CIMSS) within the Space Science and Engineering Center (SSEC) at University of Wisconsin (UW-Madison) as a collaborative effort between NOAA / NESDIS / STAR and UW-CIMSS personnel. Funding for this work came from the UK NERC National Centre for Earth Observation (NCEO), from the LSA SAF project, and from EUMETSAT. MODIS data are courtesy of NASA and SEVIRI data courtesy of EUMETSAT.

## References

- Andela, N., Kaiser, J.K, van der Werf, G., Wooster, M.J. (2015) New fire diurnal cycle characterizations to improve Fire Radiative Energy assessments made from low-Earth orbit satellites sampling, *Atmos. Chem. Phys.*, 15, 8831-8846. doi:10.5194/acp-15-8831-2015
- Aminou, D.M.A., Jacquet, B., & Pasternak, F. (1997). Characteristics of the Meteosat second generation (MSG) radiometer/imager: SEVIRI. *Sensors, Systems, and Next-Generation Satellites*, 3221, 19-31
- Aminou, D. M. A. (2002). MSG's SEVIRI instrument. *ESA Bulletin* (0376-4265), (111), 15-17.
- Andreae, M.O. (1991). Biomass Burning - Its History, Use, and Distribution and Its Impact on Environmental-Quality and Global Climate. *Global Biomass Burning*, 3-21
- Baldassarre, G., Pozzoli, L., Schmidt, C.C., Unal, A., Kindap, T., Menzel W.P., Whitburn, S., Coheur, P.-F., Kavgaci, A., and Kaiser, J.W. (2015) Using SEVIRI fire observations to drive smoke plumes in the CMAQ air quality model: the case of Antalya in 2008, *Atmos. Chem. Phys.*, 15, 8539-8558. doi:10.5194/acp-15-8539-2015
- Barnie, T. and Oppenheimer, C. (2015) Extracting High Temperature Event radiance from satellite images and correcting for saturation using Independent Component Analysis, *Remote Sensing of Environment*, 158, 1 56-68 <http://dx.doi.org/10.1016/j.rse.2014.10.023>.
- Berk, A., Anderson, G.P., Acharya, P.K., Bernstein, L.S., Muratov, L., Lee, J., Fox, M., Adler-Golden, S.M., Chetwynd, J.H., Hoke, M.L., Lockwood, R.B., Gardner, J.A., Cooley, T.W., Borel, C.C., & Lewis, P.E. (2005). MODTRAN (TM) 5, a reformulated atmospheric band model with auxiliary species and practical multiple scattering options: Update. *Algorithms and Technologies for Multispectral, Hyperspectral, and Ultraspectral Imagery XI*, 5806, 662-667
- Bucini, G., & Lambin, E. F. (2002). Fire impacts on vegetation in Central Africa: a remote-sensing-based statistical analysis. *Applied Geography*, 22(1), 27-48.
- Calle, A., Casanova, J. L., and Romo, A. (2006). Fire detection and monitoring using MSG Spinning Enhanced Visible and Infrared Imager (SEVIRI) data. *Journal of Geophysical Research: Biogeosciences* (2005–2012), 111(G4).
- Calle, A., Casanova, J.L., & Gonzalez-Alonso, F. (2009). Impact of point spread function of MSG-SEVIRI on active fire detection. *International Journal of Remote Sensing*, 30, 4567-4579

- Calle, A., Sanz, J., & Casanova, J. L. (2011). *Remote Sensing for Environmental Monitoring: Forest Fire Monitoring in Real Time*. In *Water Security in the Mediterranean Region* (pp. 47-64). Springer Netherlands.
- Carvalho, L. C., Bernardo, S. O., Orgaz, M. D. M., & Yamazaki, Y. (2010). Forest Fires Mapping and Monitoring of current and past forest fire activity from Meteosat Second Generation Data. *Environmental Modelling & Software*, 25(12), 1909-1914.
- Clerbaux, C., Boynard, A., Clarisse, L., George, M., Hadji-Lazaro, J., Herbin, H., Hurtmans, D., Pommier, M., Razavi, A., Turquety, S., Wespes, C., and Coheur, P.-F.: Monitoring of atmospheric composition using the thermal infrared IASI/MetOp sounder, *Atmos. Chem. Phys.*, 9, 6041-6054, doi:10.5194/acp-9-6041-2009, 2009.
- DaCamara, C.C. (2006). The Land Surface Analysis SAF: one year of pre-operational activity. In, *The 2006 EUMETSAT Meteorological Satellite Conference* (p. 48)
- Deneke, H.M., & Roebeling, R.A. (2010). Downscaling of METEOSAT SEVIRI 0.6 and 0.8  $\mu$  m channel radiances utilizing the high-resolution visible channel. *Atmospheric Chemistry and Physics*, 10, 9761-9772
- Derrien, M., & Le Gleau, H. (2005). Msg/Seviri Cloud Mask and Type from Safnwc. *International Journal of Remote Sensing*, 26, 4707-4732
- Dlamini, W. M. (2009). Characterization of the July 2007 Swaziland fire disaster using satellite remote sensing and GIS. *Applied geography*, 29(3), 299-307.
- Eva, H., & Lambin, E. F. (1998). Burnt area mapping in Central Africa using ATSR data. *International Journal of Remote Sensing*, 19(18), 3473-3497.
- Freeborn, P.H., Wooster, M.J., Hao, W.M., Ryan, C.A., Nordgren, B.L., Baker, S.P., & Ichoku, C. (2008). Relationships between energy release, fuel mass loss, and trace gas and aerosol emissions during laboratory biomass fires. *Journal of Geophysical Research-Atmospheres*, 113
- Freeborn, P.H., Wooster, M.J., & Roberts, G. (2011). Addressing the spatiotemporal sampling design of MODIS to provide estimates of the fire radiative energy emitted from Africa. *Remote Sensing of Environment*, 115, 475-489
- Freeborn, P.H., Wooster, M.J., Roberts, G., Malamud, B.D., & Xu, W.D. (2009). Development of a virtual active fire product for Africa through a synthesis of geostationary and polar orbiting satellite data. *Remote Sensing of Environment*, 113, 1700-1711

1057 Freeborn, P.H., Wooster, M.J., Roberts, G., & Xu, W.D. (2014a). Evaluating the  
 1058 SEVIRI Fire Thermal Anomaly Detection Algorithm across the Central African  
 1059 Republic Using the MODIS Active Fire Product. *Remote Sensing*, 6, 1890-1917  
 1060

1061 Freeborn, P.H., Wooster, M.J., Roy, D.P., & Cochrane, M.A. (2014b). Quantification  
 1062 of MODIS fire radiative power ( FRP) measurement uncertainty for use in satellite-  
 1063 based active fire characterization and biomass burning estimation. *Geophysical*  
 1064 *Research Letters*, 41, 1988-1994  
 1065

1066 Freeborn, P. H., Cochrane, M. A., & Wooster, M. J. (2014c). A Decade Long, Multi-  
 1067 Scale Map Comparison of Fire Regime Parameters Derived from Three Publically  
 1068 Available Satellite-Based Fire Products: A Case Study in the Central African  
 1069 Republic. *Remote Sensing*, 6(5), 4061-4089.  
 1070

1071 Georgiev, C.G., & Stoyanova, J.S. (2013). Parallel use of SEVIRI LSA SAF FRP and  
 1072 MPEF FIR products for fire detection and monitoring. In, *2013 EUMETSAT*  
 1073 *Meteorological Satellite Conference*. Vienna. Austria: 19th American Meteorological  
 1074 Society  
 1075

1076 Giglio, L., Descloitres, J., Justice, C.O., & Kaufman, Y.J. (2003). An enhanced  
 1077 contextual fire detection algorithm for MODIS. *Remote Sensing of Environment*, 87,  
 1078 273-282.  
 1079

1080 Giglio, L., Csiszar, I. and Justic, C. O. (2006). Global distribution and seasonality of  
 1081 active fires as observed with the Terra and Aqua Moderate Resolution Imaging  
 1082 Spectroradiometer (MODIS) sensors, *Journal of Geophysical Research:*  
 1083 *Biogeosciences* (2005–2012), 111(G2).  
 1084  
 1085

1086 Gonzalo, J., Martín-de-Mercado, G., & Valcarce, F. (2009). Space Technology for  
 1087 Disaster Monitoring, Mitigation and Damage Assessment. In *Space Technologies for*  
 1088 *the Benefit of Human Society and Earth* (pp. 305-330). Springer Netherlands

1089 Govaerts, Y., (2006) *RTMOM V0B.10 Evaluation Report*, EUMETSAT, report  
 1090 EUM/MET/DOC/06/0502, 29pp.

1091

1092 Govaerts, Y.M., M.Wooster, A.Lattanzio, & G.Roberts (2010). MSG SEVIRI *Fire*  
 1093 *Radiative Power (FRP) Algorithm Theoretical Basis Document*. Available from  
 1094 EUMETSAT LSA SAF (<http://landsaf.meteo.pt/>)  
 1095

1096 Hewison, T.J., & Muller, J. (2013). Ice Contamination of Meteosat/SEVIRI Implied  
 1097 by Intercalibration Against Metop/IASI. *Ieee Transactions on Geoscience and*  
 1098 *Remote Sensing*, 51, 1182-1186

1099  
1100 Hollingsworth, A., Engelen, R.J., Textor, C., Benedetti, A., Boucher, O., Chevallier,  
1101 F., Dethof, A., Elbern, H., Eskes, H., Flemming, J., Granier, C., Kaiser, J.W.,  
1102 Morcrette, J.J., Rayner, P., Peuch, V.H., Rouil, L., Schultz, M.G., Simmons, A.J., &  
1103 Consortium, G. (2008). Toward a monitoring and forecasting system for atmospheric  
1104 composition: The GEMS project. *Bulletin of the American Meteorological Society*,  
1105 89, 1147-1164  
1106  
1107 Just, D. (2000). Sevir level 1.5 data. *First Msg Rao Workshop*, 452, 29-37  
1108  
1109 Just, D., Gutiérrez, R., Roveda, F., & Steenbergen, T. (2014). Meteosat third  
1110 generation imager: simulation of the flexible combined imager instrument chain.  
1111 In SPIE Remote Sensing (pp. 92410E-92410E). *International Society for Optics and*  
1112 *Photonics*, October 2014.  
1113  
1114 Kaiser, J.W., Heil, A., Andreae, M.O., Benedetti, A., Chubarova, N., Jones, L.,  
1115 Morcrette, J.J., Razinger, M., Schultz, M.G., Suttie, M., & van der Werf, G.R. (2012).  
1116 Biomass burning emissions estimated with a global fire assimilation system based on  
1117 observed fire radiative power. *Biogeosciences*, 9, 527-554  
1118  
1119 Koutsias, N., Arianmoutsou, M., Kallimanis, A. S., Mallinis, G., Halley, J. M., and  
1120 Dimopoulos, P. (2012) Where did the fires burn in Peloponnese, Greece the summer  
1121 of 2007? Evidence for a synergy of fuel and weather. *Agricultural and Forest*  
1122 *Meteorology*, 156. 41-53.  
1123  
1124 Kremens, R.L., Dickinson, M.B., & Bova, A.S. (2012). Radiant flux density, energy  
1125 density and fuel consumption in mixed-oak forest surface fires. *International Journal*  
1126 *of Wildland Fire*, 21, 722-730  
1127  
1128 Libonati, R., DaCamara, C.C., Pereira, J.M.C., & Peres, L.F. (2010). Retrieving  
1129 middle-infrared reflectance for burned area mapping in tropical environments using  
1130 MODIS. *Remote Sensing of Environment*, 114, 831-843  
1131  
1132 Liu, Y., Kahn, R. A., Chaloulakou, A., & Koutrakis, P. (2009). Analysis of the impact  
1133 of the forest fires in August 2007 on air quality of Athens using multi-sensor aerosol  
1134 remote sensing data, meteorology and surface observations. *Atmospheric*  
1135 *Environment*, 43(21), 3310-3318.  
1136  
1137 Mayaux, P., Bartholome, E., Fritz, S., & Belward, A. (2004). A new land-cover map  
1138 of Africa for the year 2000. *Journal of Biogeography*, 31, 861-877  
1139  
1140 MeteoFrance (2010). Algorithm theoretical basis document for cloud products



1141 Pereira, G., Shimabukuro, Y.E., Moraes, E.C., Freitas, S.R., Cardozo, F.S., & Longo,  
 1142 K.M. (2011). Monitoring the transport of biomass burning emission in South  
 1143 America. *Atmospheric Pollution Research*, 2, 247-254  
 1144

1145 Murphy, D. (2013). EUMETSAT Geostationary Meteorological Satellite Programs.  
 1146 In *Handbook of Satellite Applications* (pp. 991-1019). Springer New York.  
 1147

1148 Pausas, J. G., & Fernández-Muñoz, S. (2012). Fire regime changes in the Western  
 1149 Mediterranean Basin: from fuel-limited to drought-driven fire regime. *Climatic*  
 1150 *Change*, 110(1-2), 215-226.  
 1151

1152 Prins, E.M., Feltz, J.M., Menzel, W.P., & Ward, D.E. (1998). An overview of GOES-  
 1153 8 diurnal fire and smoke results for SCAR-B and 1995 fire season in South America.  
 1154 *Journal of Geophysical Research-Atmospheres*, 103, 31821-31835  
 1155

1156 Poupkou, A., Markakis, K., Liora, N., Giannaros, T. M., Zanis, P., Im, U., ... &  
 1157 Zerefos, C. (2014). A modeling study of the impact of the 2007 Greek forest fires on  
 1158 the gaseous pollutant levels in the Eastern Mediterranean. *Atmospheric Research*.  
 1159

1160 Qin, Z., & Karnieli, A. (1999). Progress in the remote sensing of land surface  
 1161 temperature and ground emissivity using NOAA-AVHRR data. *International Journal*  
 1162 *of Remote Sensing*, 20(12), 2367-2393  
 1163

1164 Reid, J.S., Hyer, E.J., Prins, E.M., Westphal, D.L., Zhang, J.L., Wang, J., Christopher,  
 1165 S.A., Curtis, C.A., Schmidt, C.C., Eleuterio, D.P., Richardson, K.A., & Hoffman, J.P.  
 1166 (2009). Global Monitoring and Forecasting of Biomass-Burning Smoke: Description  
 1167 of and Lessons From the Fire Locating and Modeling of Burning Emissions  
 1168 (FLAMBE) Program. *Ieee Journal of Selected Topics in Applied Earth Observations*  
 1169 *and Remote Sensing*, 2, 144-162  
 1170

1171 Remy, S., & Kaiser, J.W. (2014). Daily global fire radiative power fields estimation  
 1172 from one or two MODIS instruments. *Atmos. Chem. Phys. Discuss.*, 14, 20805-20844  
 1173 Roberts, G., & Wooster, M. (2014). Development of a multi-temporal Kalman filter  
 1174 approach to geostationary active fire detection & fire radiative power (FRP)  
 1175 estimation. *Remote Sensing of Environment*, 152, 392-412  
 1176

1177 Roberts, G., Wooster, M. J., Xu, W., Freeborn, P. H., Morcrette, J-J., Jones, L.,  
 1178 Benedetti, A. and Kaiser, J. (2015) LSA SAF Meteosat FRP Products: Part 2 –  
 1179 Evaluation and demonstration of use in the Copernicus Atmosphere Monitoring  
 1180 Service (CAMS) *Atmos. Chem. Phys. Discuss.*, 15, 15909-15976, 2015  
 1181

1182 Roberts, G., Wooster, M., Freeborn, P.H., & Xu, W. (2011). Integration of  
 1183 geostationary FRP and polar-orbiter burned area datasets for an enhanced biomass  
 1184 burning inventory. *Remote Sensing of Environment*, 115, 2047-2061

1185  
1186 Roberts, G., Wooster, M.J., & Lagoudakis, E. (2009a). Annual and diurnal african  
1187 biomass burning temporal dynamics. *Biogeosciences*, 6, 849-866  
1188  
1189 Roberts, G., Wooster, M.J., Lagoudakis, E., Freeborn, P., & Xu, W. (2009b).  
1190 Continental Africa Biomass Burning Temporal Dynamics derived from MSG  
1191 SEVIRI. 2009 *Ieee International Geoscience and Remote Sensing Symposium*, Vols 1-  
1192 5, 1458-1461  
1193  
1194 Roberts, G., Wooster, M.J., Perry, G.L.W., Drake, N., Rebelo, L.M., & Dipotso, F.  
1195 (2005). Retrieval of biomass combustion rates and totals from fire radiative power  
1196 observations: Application to southern Africa using geostationary SEVIRI imagery.  
1197 *Journal of Geophysical Research*, 110, D21, doi: 10.1029/2005JD006018  
1198  
1199 Roberts, G.J., & Wooster, M.J. (2008). Fire detection and fire characterization over  
1200 Africa using Meteosat SEVIRI. *Ieee Transactions on Geoscience and Remote*  
1201 *Sensing*, 46, 1200-1218  
1202  
1203 Roberts, G., and Wooster, M.J. (2014) Development of a multi-temporal Kalman  
1204 filter approach to geostationary active fire detection and fire radiative power (FRP)  
1205 estimation, *Remote Sensing of Environment*, 152, 92-412,  
1206 <http://dx.doi.org/10.1016/j.rse.2014.06.020>.  
1207  
1208 Ross, A.N., Wooster, M.J., Boesch, H., & Parker, R. (2013). First satellite  
1209 measurements of carbon dioxide and methane emission ratios in wildfire plumes.  
1210 *Geophysical Research Letters*, 40, 4098-4102  
1211  
1212 Schmetz, J., Pili, P., Tjemkes, S., Just, D., Kerkmann, J., Rota, S., & Ratier, A.  
1213 (2002). An introduction to Meteosat Second Generation (MSG). *Bulletin of the*  
1214 *American Meteorological Society*, 83, 977-992  
1215  
1216 Schroeder, W., Prins, E., Giglio, L., Csiszar, I., Schmidt, C., Morisette, J., & Morton,  
1217 D. (2008). Validation of GOES and MODIS active fire detection products using  
1218 ASTER and ETM plus data. *Remote Sensing of Environment*, 112, 2711-2726  
1219  
1220 Schroeder, W., Oliva, P., Giglio, L., & Csiszar, I. A. (2014). The New VIIRS 375m  
1221 active fire detection data product: Algorithm description and initial  
1222 assessment. *Remote Sensing of Environment*, 143, 85-96.  
1223  
1224 Sofiev, M., Vankevich, R., Lotjonen, M., Prank, M., Petukhov, V., Ermakova, T.,  
1225 Koskinen, J., & Kukkonen, J. (2009). An operational system for the assimilation of  
1226 the satellite information on wild-land fires for the needs of air quality modelling and  
1227 forecasting. *Atmospheric Chemistry and Physics*, 9, 6833-6847  
1228

- Trigo, I. F., Dacamara, C. C., Viterbo, P., Roujean, J. L., Olesen, F., Barroso, C., ... & Arboleda, A. (2011). The satellite application facility for land surface analysis. *International Journal of Remote Sensing*, 32(10), 2725-2744.
- Turquety, S., Menut, L., Bessagnet, B., Anav, A., Viovy, N., Maignan, F., & Wooster, M. (2014). APIFLAME v1. 0: high-resolution fire emission model and application to the Euro-Mediterranean region. *Geoscientific Model Development*, 7(2), 587-612.
- van der Werf, G.R., Randerson, J.T., Collatz, G.J., & Giglio, L. (2003). Carbon emissions from fires in tropical and subtropical ecosystems. *Global Change Biology*, 9, 547-562
- van der Werf, G.R., Randerson, J.T., Giglio, L., Collatz, G.J., Kasibhatla, P.S., & Arellano, A.F. (2006). Interannual variability in global biomass burning emissions from 1997 to 2004. *Atmospheric Chemistry and Physics*, 6, 3423-3441
- Vermote, E., Ellicott, E., Dubovik, O., Lapyonok, T., Chin, M., Giglio, L., & Roberts, G.J. (2009). An approach to estimate global biomass burning emissions of organic and black carbon from MODIS fire radiative power. *Journal of Geophysical Research-Atmospheres*, 114
- Wooster, M.J., Roberts, G., Perry, G.L.W., & Kaufman, Y.J. (2005). Retrieval of biomass combustion rates and totals from fire radiative power observations: FRP derivation and calibration relationships between biomass consumption and fire radiative energy release. *Journal of Geophysical Research-Atmospheres*, 110
- Wooster, M.J., Zhukov, B., & Oertel, D. (2003). Fire radiative energy for quantitative study of biomass burning: derivation from the BIRD experimental satellite and comparison to MODIS fire products. *Remote Sensing of Environment*, 86, 83-107
- Wooster, M. J., Xu, W., & Nightingale, T. (2012). Sentinel-3 Giglio *et al.*, 2003; active fire detection and FRP product: Pre-launch algorithm development and performance evaluation using MODIS and ASTER datasets. *Remote Sensing of Environment*, 120, 236-254.
- Wooster, M. J., Roberts, G., Smith, A. M., Johnston, J., Freeborn, P., Amici, S., & Hudak, A. T. (2013). Thermal Remote Sensing of Active Vegetation Fires and Biomass Burning Events. In *Thermal Infrared Remote Sensing* (pp. 347-390). Springer Netherlands.
- Xu, W., Wooster, M.J., Roberts, G., & Freeborn, P. (2010). New GOES imager algorithms for cloud and active fire detection and fire radiative power assessment across North, South and Central America. *Remote Sensing of Environment*, 114, 1876-1895

1273 Zhang, X.Y., Kondragunta, S., Ram, J., Schmidt, C., & Huang, H.C. (2012). Near-  
1274 real-time global biomass burning emissions product from geostationary satellite  
1275 constellation. *Journal of Geophysical Research-Atmospheres*, 117  
1276  
1277 Zhukov, B., Lorenz, E., Oertel, D., Wooster, M., & Roberts, G. (2006). Spaceborne  
1278 detection and characterization of fires during the bi-spectral infrared detection (BIRD)  
1279 experimental small satellite mission (2001-2004). *Remote Sensing of Environment*,  
1280 100, 29-51  
1281

## TABLES

Table 1. Spectral Bands of Meteosat SEVIRI

Channel No.	Spectral Band ( $\mu\text{m}$ )	Band Characteristics (wavelength, $\mu\text{m}$ )			Main Observational Applications
		Centre	Min	Max	
1	VIS0.6	0.635	0.56	0.71	Surface, clouds, wind fields
2	VIS0.8	0.81	0.74	0.88	Surface, clouds, wind fields
3	NIR1.6	1.64	1.50	1.78	Surface, cloud phase
4	IR3.9	3.90	3.48	4.36	Surface, clouds, wind fields
5	WV6.2	6.25	5.35	7.15	Water vapour, high level clouds, atmospheric instability
6	WV7.3	7.35	6.85	7.85	Water vapor, atmospheric instability
7	IR8.7	8.70	8.30	9.1	Surface, clouds, atmospheric instability
8	IR9.7	9.66	9.38	9.94	Ozone
9	IR10.8	10.80	9.80	11.80	Surface, clouds, wind fields, atmospheric instability
10	IR12.0	12.00	11.00	13.00	Surface, clouds, atmospheric instability
11	IR13.4	13.40	12.40	14.40	Cirrus cloud height, atmospheric instability
12	HRV	Broadband (about 0.4 - 1.1 $\mu\text{m}$ )	Surface, clouds		

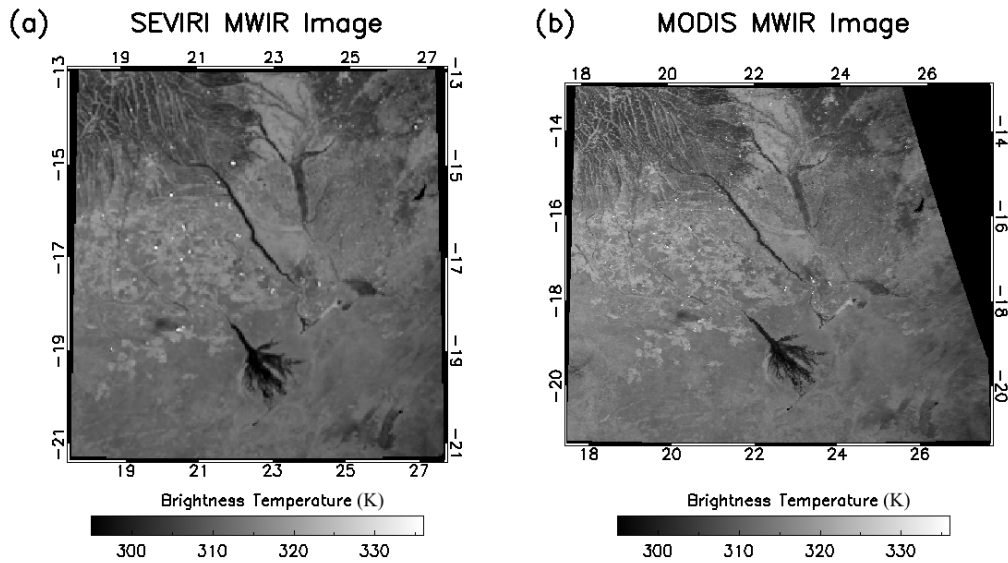
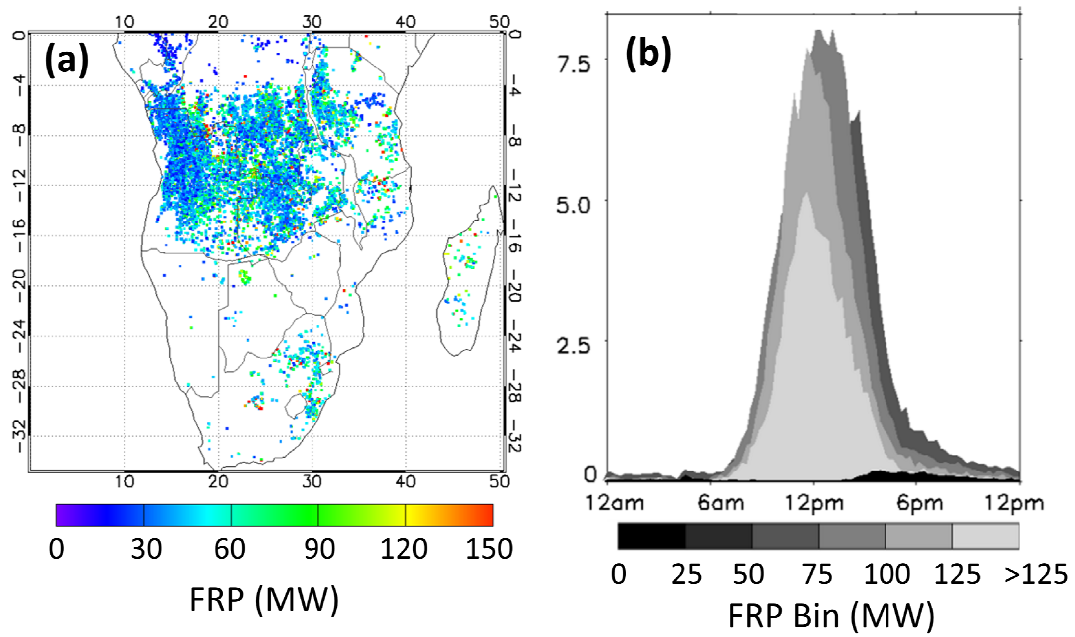


Figure 1. Near simultaneous MWIR channel imagery of fires in southern Africa from (a) SEVIRI (IR3.9) and (b) MODIS (Band 21). These image subsets show pixels with elevated MWIR brightness temperatures as bright, and almost all of these are likely caused by actively burning fires. The area shown includes the Okavango delta wetland (around 250 km long), which shows up as relatively cooler than the surrounding dry land. The SEVIRI data were collected at 12:50 UTC on 17<sup>th</sup> August 2007, and the MODIS data around ten minutes earlier. The polar orbiting MODIS and geostationary SEVIRI data are not exactly co-registered, but cover approximately the same area. Whilst the increased spatial resolution of the MODIS data is clear and allows more fires to be visually identified via their elevated MWIR signals, many of the fires can also clearly be seen in the SEVIRI imagery (albeit with lower MWIR brightness temperatures since the fires are filling a lower proportion of the larger SEVIRI pixel than the matching MODIS pixels). SEVIRI provides 96 images per day (one every 15 minutes) at a consistent view zenith angle. At this latitude up MODIS provides up to four images per day, though some of these will be at extreme view zenith angles up to 65° under which conditions the MODIS spatial fidelity is far reduced, with each pixel covering approximately the same ground area as does a SEVIRI pixel (Freeborn *et al.*, 2011). The local afternoon imaging time of MODIS Aqua, as used here, is also relatively close to the typical peak of the fire diurnal cycle (Roberts *et al.*, 2009a), but the times of the other MODIS overpasses are significantly distant from this.

1316



1317

1318

1319 Figure 2: Example data extracted from the LSA SAF Meteosat SEVIRI FRP-PIXEL  
 1320 product. (a) Active fire locations and their FRP as measured on 17<sup>th</sup> July 2009 over  
 1321 southern Africa. (b) The same data but now shown as the diurnal cycle of FRP,  
 1322 binned into 25 MW increments. These data indicate that the individual fire pixel FRP  
 1323 values recorded on this date almost all lay below 150 MW, and that the peak of the  
 1324 diurnal cycle generally occurred earlier in the day for higher FRP fire pixels.

1325

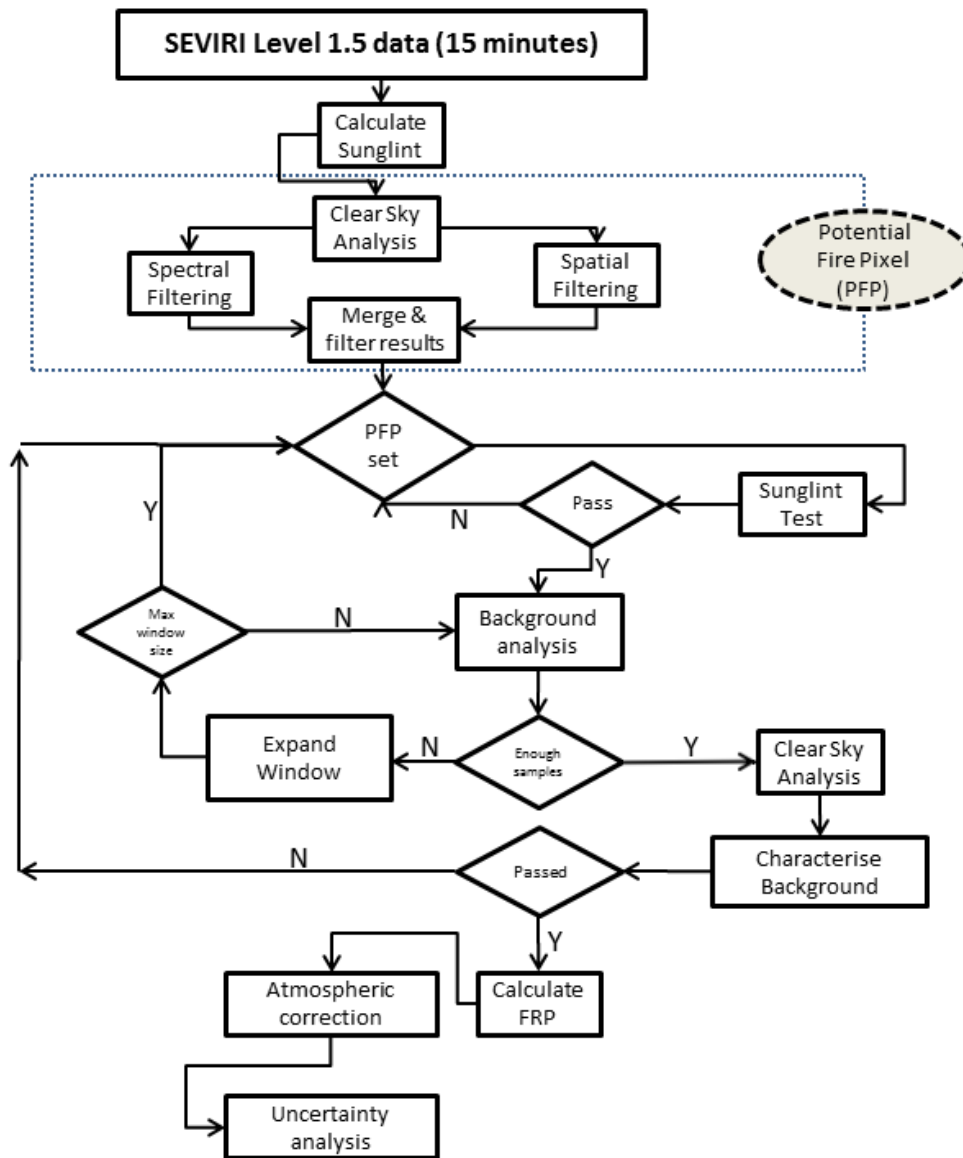


Figure 3: Flowchart illustrating the FRP-PIXEL product processing chain, which uses the operational geostationary ‘Fire Thermal Anomaly’ (FTA) algorithm described herein. The processing chain acts upon the input Level 1.5 data from each SEVIRI imaging slot independently, and the procedures outlined by the blue dotted box are those involved in selection of the potential fire pixels (PFPs). These PFPs are then subject to a series of thresholding procedures based on spatially varying ‘contextual’ thresholds, used to determine whether or not each FPF can be confirmed as a true active fire pixel and have its FRP assessed.



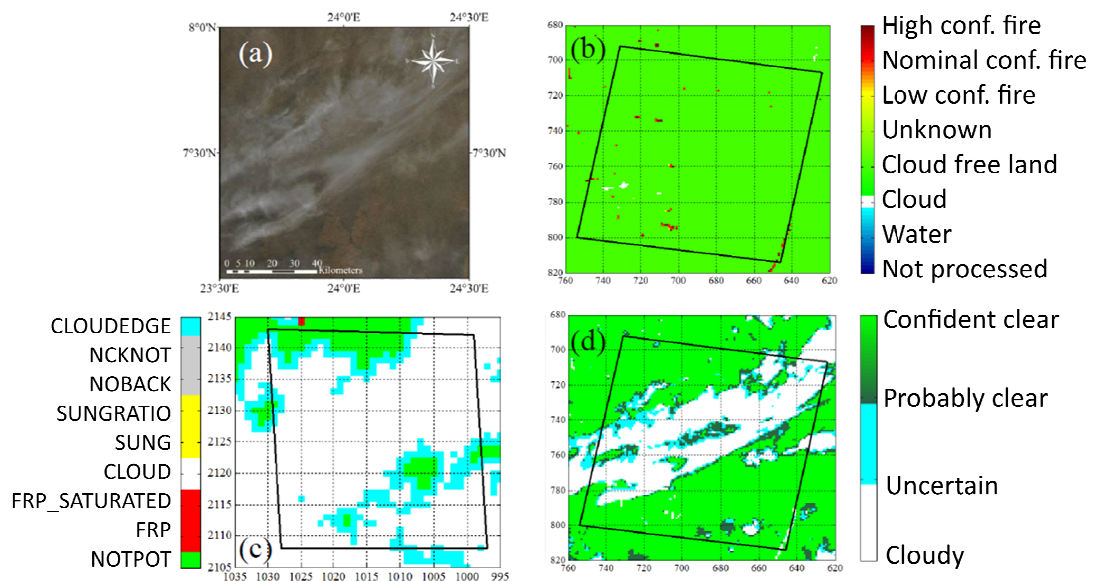


Figure 4: Simultaneous data collected by the Aqua MODIS and Meteosat SEVIRI instruments over a  $1^{\circ} \times 1^{\circ}$  region of Central African Republic at 12:00 UTC on 11 January 2009. (a) 500 m spatial resolution MODIS Aqua true colour composite, (b) MODIS fire mask retrieved from the coincident MYD14 Active Fire and Thermal Anomaly product, (c) the status flags (Table S1 in Supplementary Materials) retrieved from the coincident SEVIRI FRP-PIXEL quality file, and (d) the MODIS cloud mask retrieved from the coincident MYD35 MODIS Cloud Product. The MODIS true colour composite image has been reprojected into geographic coordinates, and this area is shown boxed on the other products (shown in their native image coordinate systems). It is apparent that the geographically widespread, but somewhat transparent, cloud shown in the MODIS colour composite in (a) is widely detected by the MODIS MYD35 cloud mask (d) and by the adapted CMA Cloud Mask used in the FRP-PIXEL products (c). However, the MODIS cloud mask used in the MODIS fire product (b) is specified such that it does not detect such thin cloud and allows fires burning underneath to remain detectable. Far less cloud can be seen to be detected by this mask than by either other the other two masks. Figure adapted from Freeborn *et al.* (2014a), who go onto confirm the very strong sensitivity of the SEVIRI CMA mask of Derrien and Le Gleau (2005) compared to that of the MODIS Active Fire Product cloud mask.

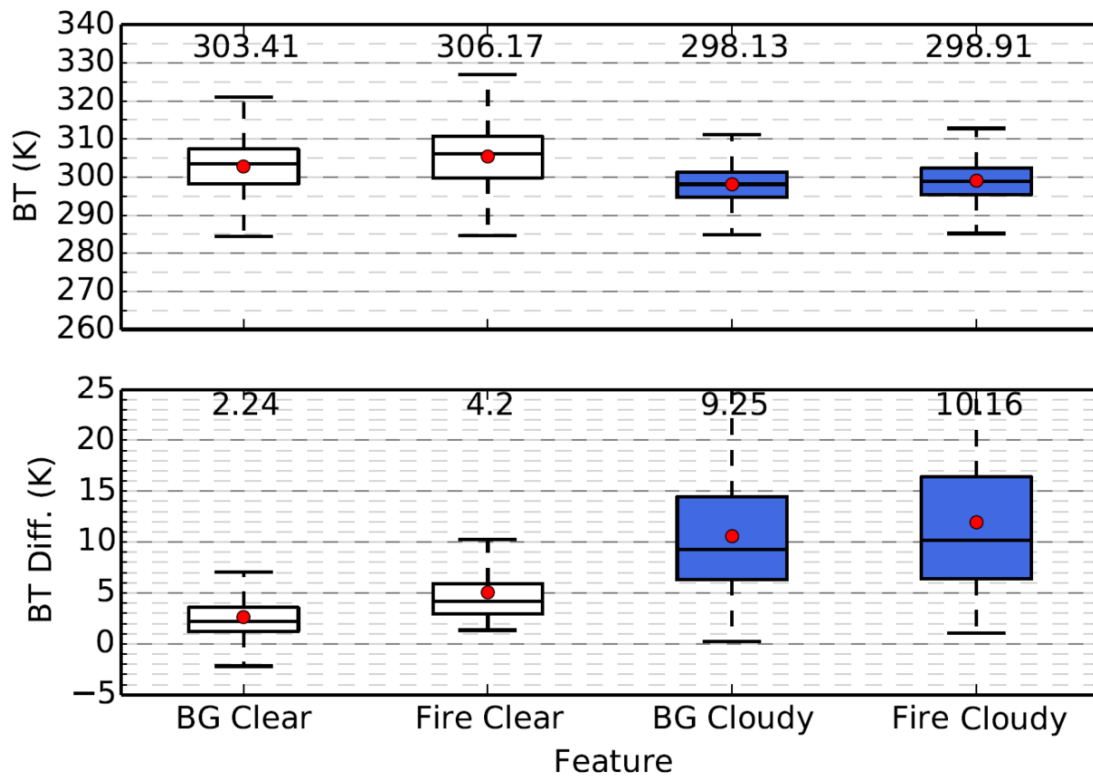


Figure 5. Examination of signals from fires burning under clear sky and thin cloud, along with their background windows (BG). Potential fire pixel (Fire) and background (BG) signal box plots for IR3.9 Brightness Temperature (BT) and IR3.9 - IR10.8 BT differences calculated using five days of SEVIRI daytime data (8<sup>th</sup>-12<sup>th</sup> August 2014) over the southern Africa. Boxplot follows standard conventions, with the bar representing the median and red dot the mean. The figure above each box plot reports the actual median value.

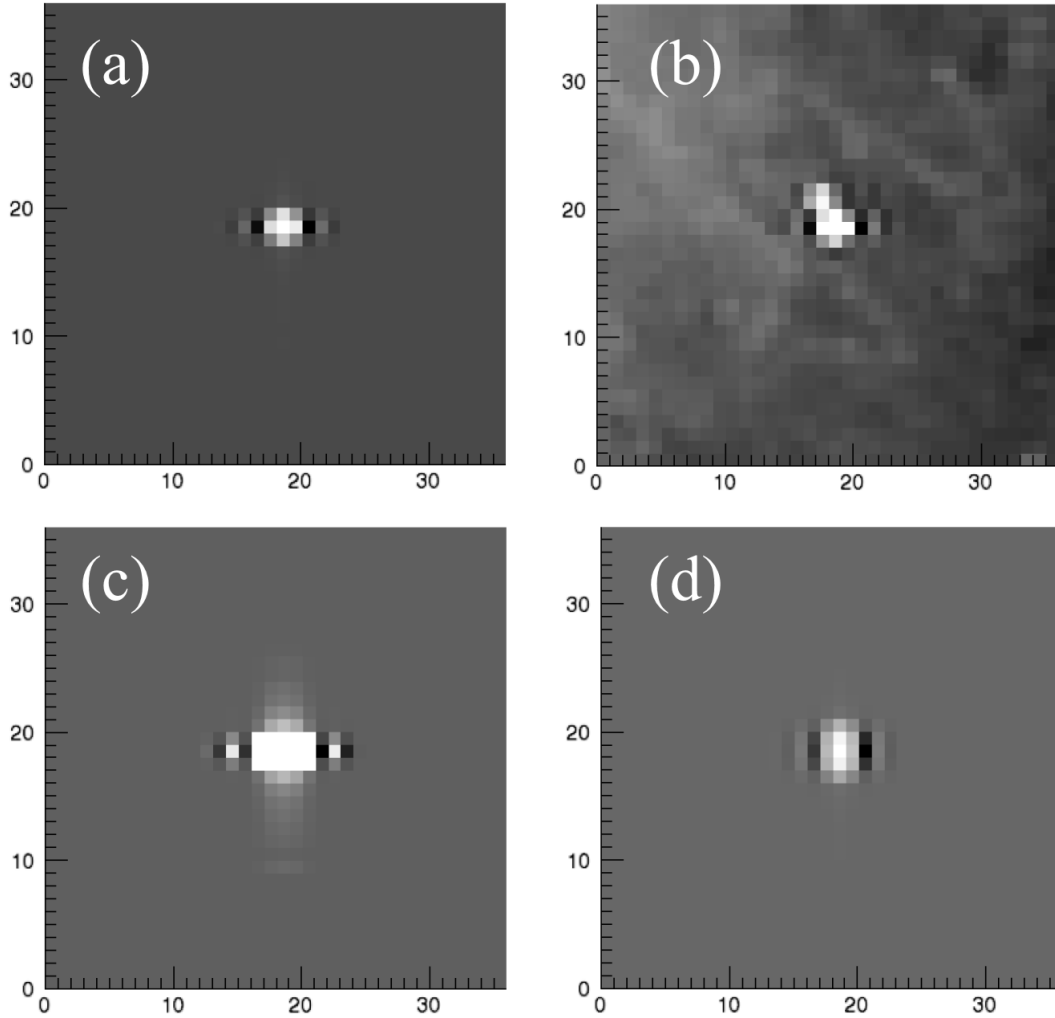
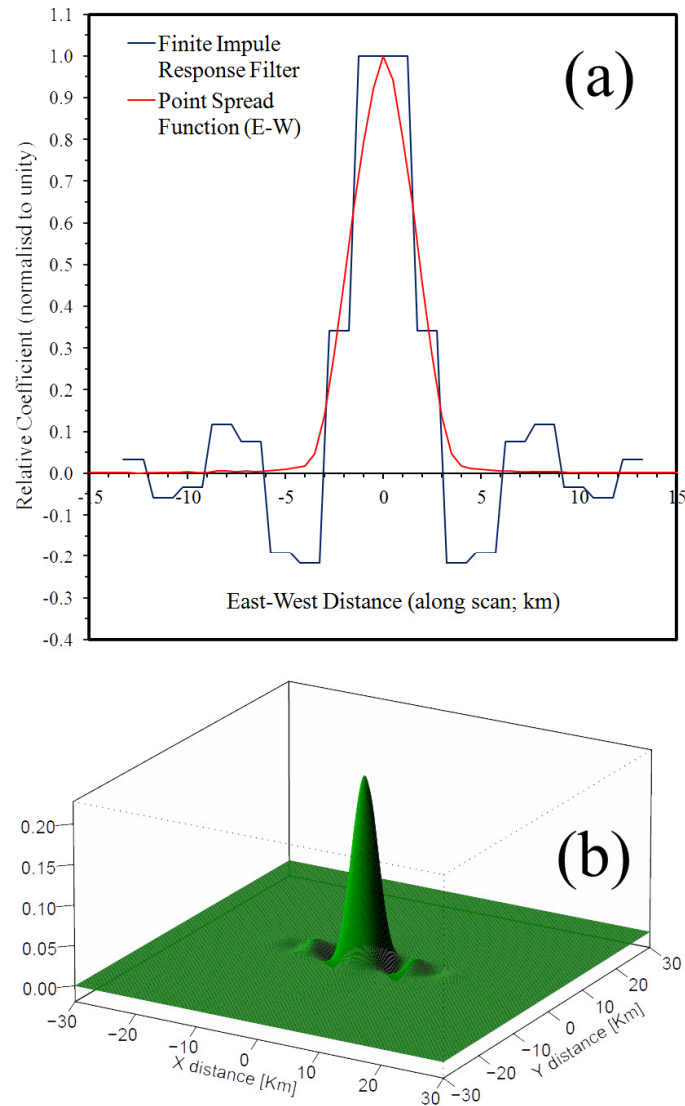


Figure 6: Simulated SEVIRI IR3.9 (MWIR) imagery of active fires, shown in comparison to real imagery. Images are scaled with the highest brightness temperature in the images shown white, and the lowest black. x and y axes are in SEVIRI image column and row coordinates. (a) is a simulated MWIR view of a 350 MW fire contained within the ground area of a single SEVIRI 3 km pixel and with the convolved filter shown in Figure 7 applied. The fire signal appears smeared across many pixels, and the result appears similar to typical SEVIRI imagery of active fires shown in (b), but noting that the dominantly along-scan nature of the smearing may not be so apparent in real SEVIRI imagery due to the pixel geolocation processes performed during the level 1.0 to level 1.5 pre-processing procedures. (c) and (d) show simulation of larger fires stretching across three 350 MW SEVIRI pixels in the E-W and N-S directions respectively, with the impact of the filtering shown to be dependent upon the fire orientation with respect to the SEVIRI scan process. The simulations are indicative only, with a uniform surface temperature, atmospheric transmission and emissivity assumed, and the sub-pixel fire of fixed FRP located at the scene centre.



1387

1388

1389 Figure 7: (a) The E-W point spread function of SEVIRI (at sub-satellite point) and the  
 1390 finite impulse response (FIR) function. The latter is applied to Level 1.0 data before  
 1391 conversion to level 1.5. Both are shown here normalised to unity. Note the negative  
 1392 side lobes of the FIR filter. (b) Convolution of the FIR filter and the E-W and N-S  
 1393 SEVIRI point spread function (PSF) used in the simulation of active fire observations  
 1394 (Figure 6).

1395

1396

1397

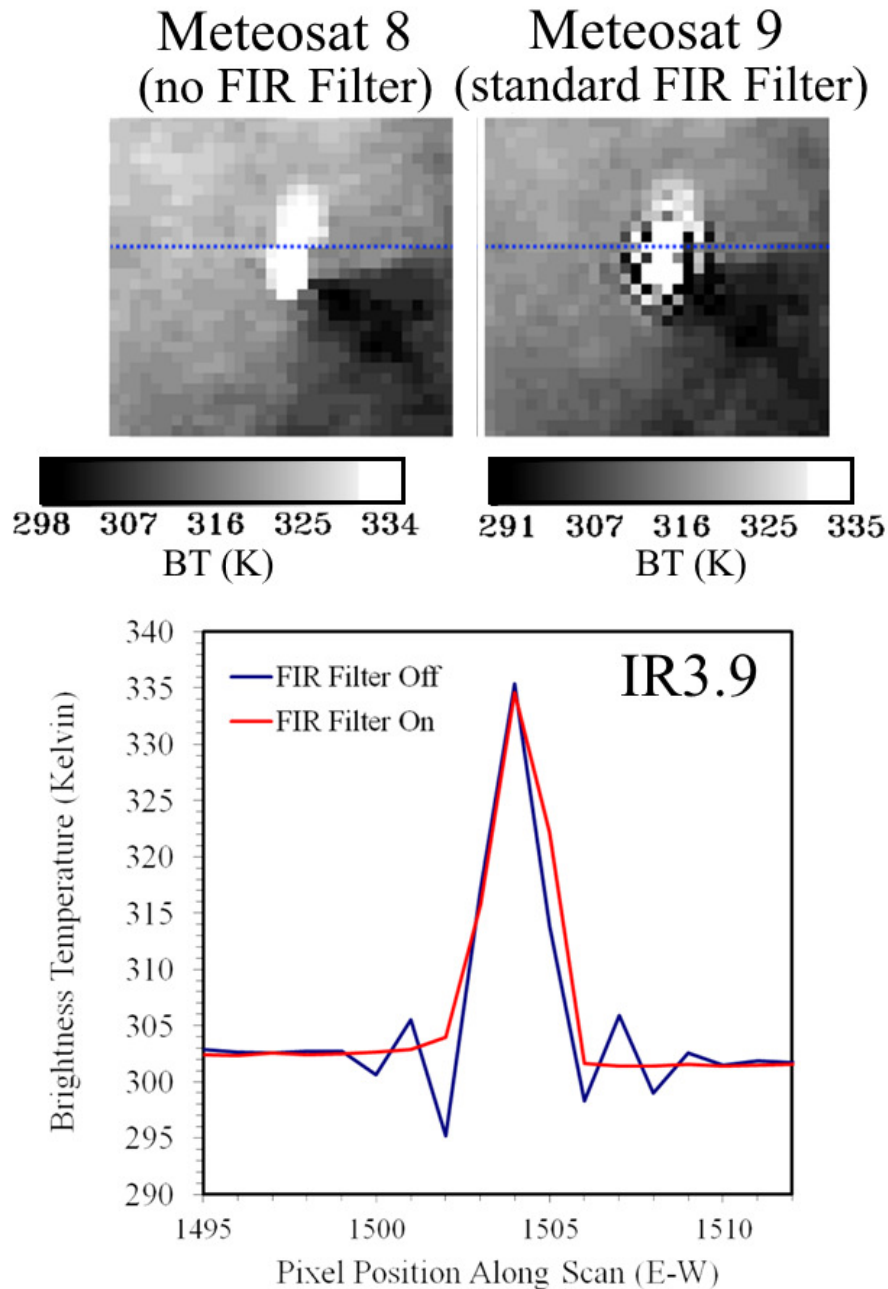


Figure 8: Near simultaneous Meteosat-8 and -9 Band 4 (MWIR) Imagery of a large, intensely burning (high FRP) fire in southern Africa taken on 3<sup>rd</sup> September 2007 during Meteosat-8 'Special operations' when application of the FIR filter was removed temporarily. Data appear quite different to that collected with the normally operating Meteosat-9.

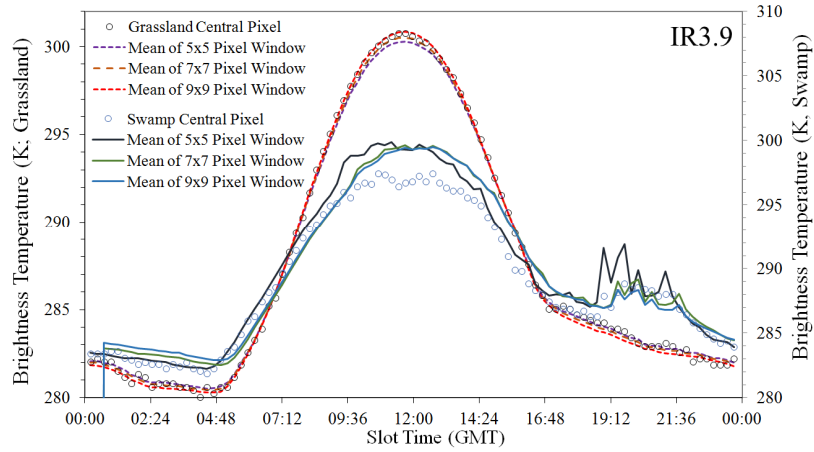


Figure 9: Demonstration of the ability to estimate the SEVIRI IR3.9 (MWIR) brightness temperature of the central pixel in a 5×5, 7×7 and 9×9 pixel window, using the mean of the remaining 'background window' pixels. Results for two different landcover types are shown from the GLC2000 database, grassland (plotted on left hand y-axis) and swamp (plotted on right hand y-axis).

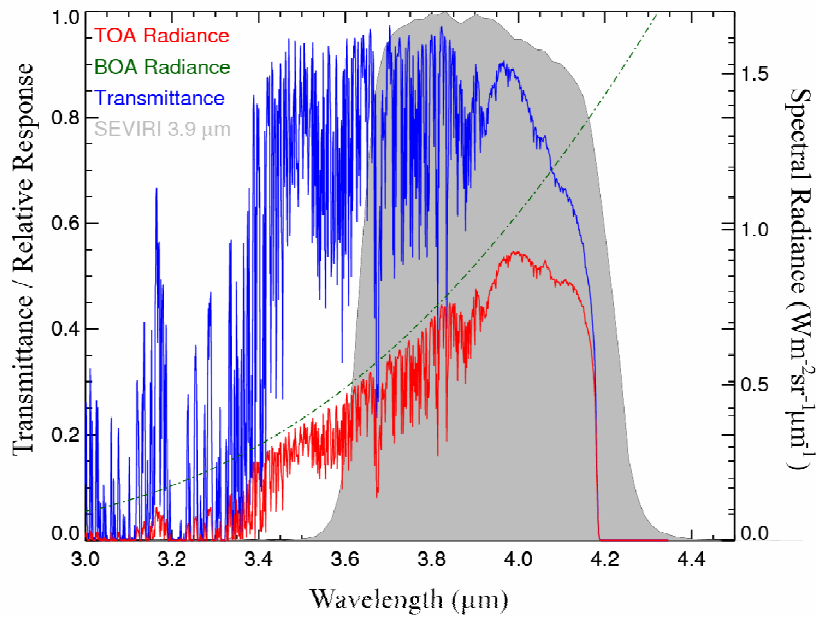


Figure 10: SEVIRI IR3.9 (MWIR) band spectral response function, with example atmospheric transmittance calculated across the 3.0 - 4.5  $\mu\text{m}$  wavelength range assuming a standard atmosphere (Berk *et al.*, 2005), plotted on the left y-axis. Also shown, plotted on the right y-axis, are the bottom-of-atmosphere (BOA) thermal emittance for a 310 K blackbody, along with the top-of-atmosphere (TOA) equivalent after the emitted radiation has passed through the intervening atmosphere to space. Simulations performed using the MODTRAN 5 radiative transfer code (Berk *et al.*, 2005 and the US Standard Atmosphere).

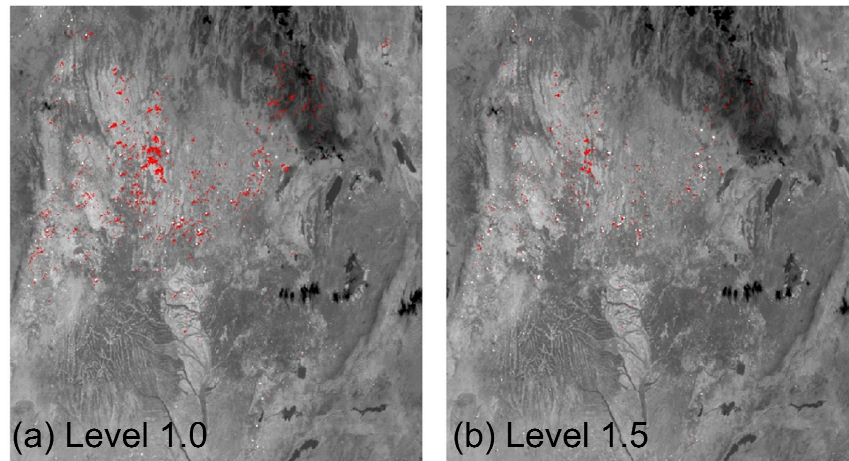
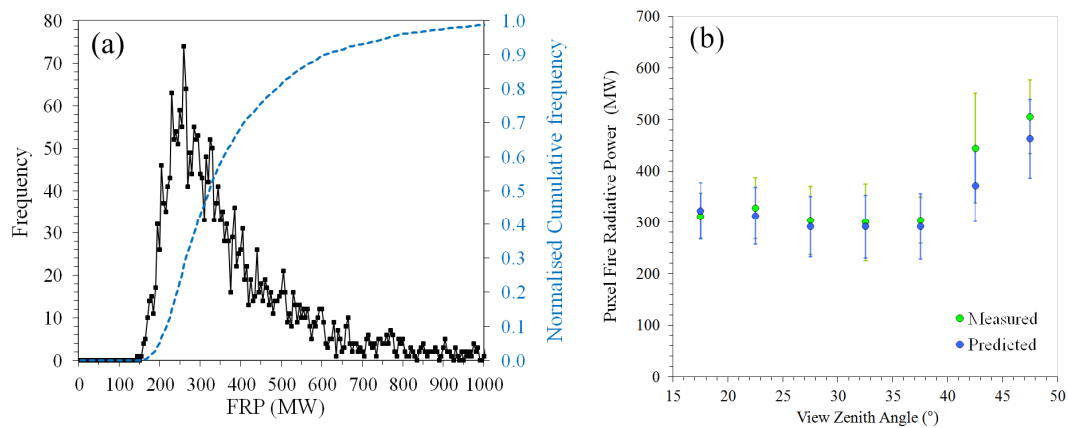


Figure 11: Impact of IR3.9 channel saturation in SEVIRI level 1.0 and level 1.5 data. Typically a maximum of only a few percent of active fire pixels are saturated in any particular SEVIRI image, but the exact proportion is dependent on data pre-processing levels. Here in red we show the spatial distribution of saturated active fire pixels in (a) level 1.0 and (b) level 1.5 SEVIRI data collected over a 2-day (48 hr) period in a region of southern Africa (16<sup>th</sup> and 17<sup>th</sup> July, 2014). Twice as many pixels are saturated in the level 1.0 across these two days (shown by a 10-bit DN of 1023; n=2797) than are apparent in the level 1.5 data (shown by a maximum brightness temperature recordable in the IR3.9 band; n=1390). The background imagery on which the saturated pixels are displayed is an IR3.9 image acquired on the 17<sup>th</sup> July at 13:00 hrs (UTC).

1439



1440

1441

1442

1443 Figure 12. Occurrence and impact of SEVIRI IR3.9 saturation. (a) Frequency  
 1444 distribution and normalised cumulative frequency of the FRP recorded at detected  
 1445 active fire pixels that would have been saturated under normal SEVIRI operating  
 1446 conditions, but which remained unsaturated during the low-gain 'Special Operation' of  
 1447 the IR3.9 band of Meteosat-8 SEVIRI. Pixels with FRP > 1000 MW are shown due to  
 1448 their extremely low frequency, though one pixel with an FRP approaching 2000 MW  
 1449 was seen (see main text). (b) Median FRP recorded at active fire pixels which would  
 1450 have been saturated had Meteosat-8 SEVIRI been operating in normal gain mode, but  
 1451 which when observed during the low-gain IR3.9 band 'Special Operation' of  
 1452 Meteosat-8 SEVIRI remained unsaturated. Data are stratified by view zenith angle.  
 1453 Also shown are the  $\pm 1$  mean absolute deviation from the median, and the predictions  
 1454 of FRP made when the actual fire pixel IR3.9 spectral radiance is replaced with a  
 1455 fixed value of  $4.08 \text{ mW m}^{-2} \text{ sr}^{-1} (\text{cm}^{-1})^{-1}$  to represent the adjustment applied to  
 1456 saturated pixels in normal mode level 1.5 SEVIRI data during FRP-PIXEL processing  
 1457 (see Section 5).

1458

1459

1460

1461



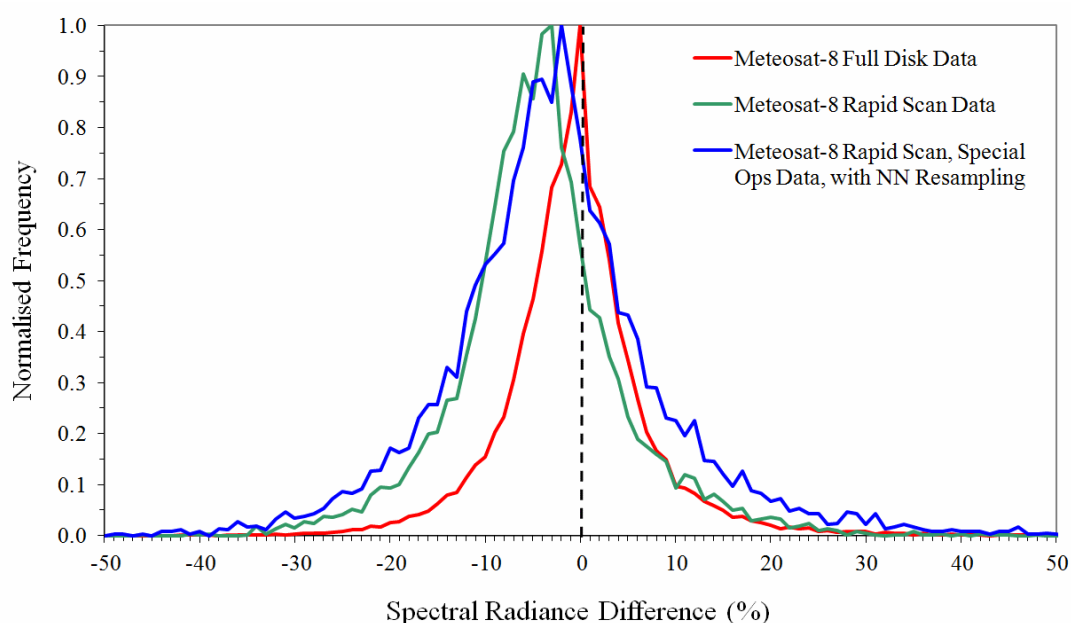


Figure 13: Comparison of SEVIRI IR3.9 band spectral radiance differences recorded at active fire pixels observed simultaneously by Meteosat-9 operated in standard mode full disk viewing, and Meteosat-8 operated in both standard mode and a number of 'Special Operations' modes. The red line shows the difference between Meteosat-8 and -9 signals when the former is operated in normal mode, with no time difference between observations, the green line when Meteosat-8 Rapid Scan mode was used, which resulted in time differences of 50 - 65 secs between matched observations of the two satellites, and the blue line when Meteosat-8 Rapid Scan data were processed without the FIR filter and with a nearest neighbour geometric resampling scheme (rather than the normal bi-cubic function). From these intercomparisons, estimates of the radiometric uncertainties introduced by the SEVIRI level 1.0 to level 1.5 pre-processing operations were deduced for use in FRP uncertainty specification (Section 5).

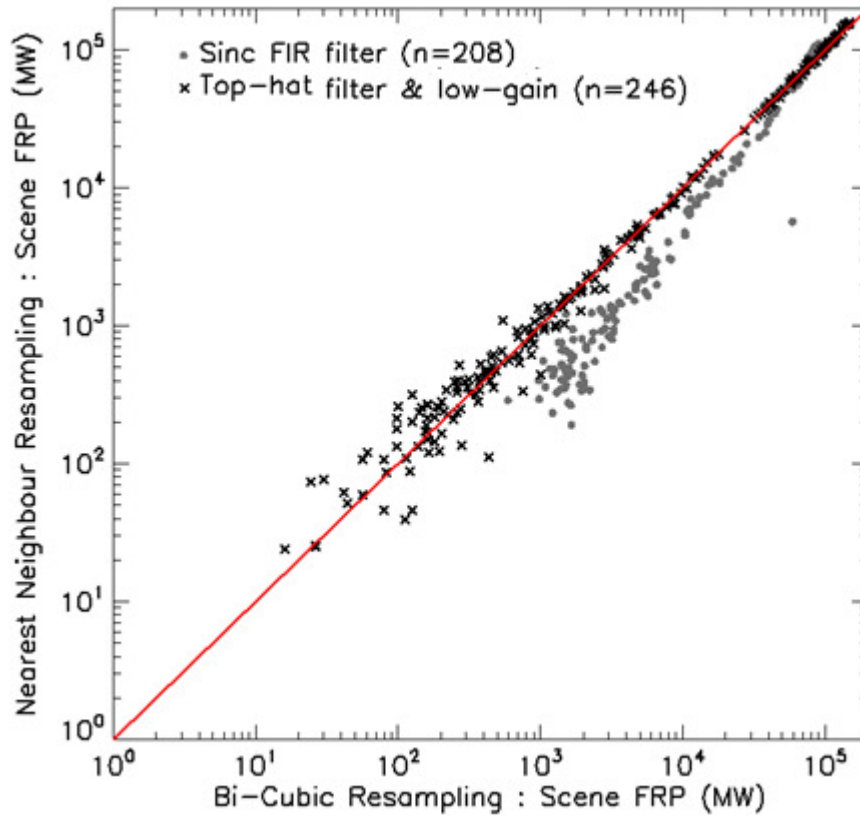


Figure 14: Cumulative FRP (MW) in a scene as measured by Meteosat-8 operating in 'special operations mode' across the region of the Rapid Scan observations ( $3^{\circ}$  N to  $33^{\circ}$  S) when data were delivered using different geometric resampling schemes (nearest neighbour and bi-cubic convolution) and image processing filters (standard Sinc function shown in Figure 7, and 'top-hat' which equates to no significant digital filtering). Data were collected between 3<sup>rd</sup> – 7<sup>th</sup> September 2007.

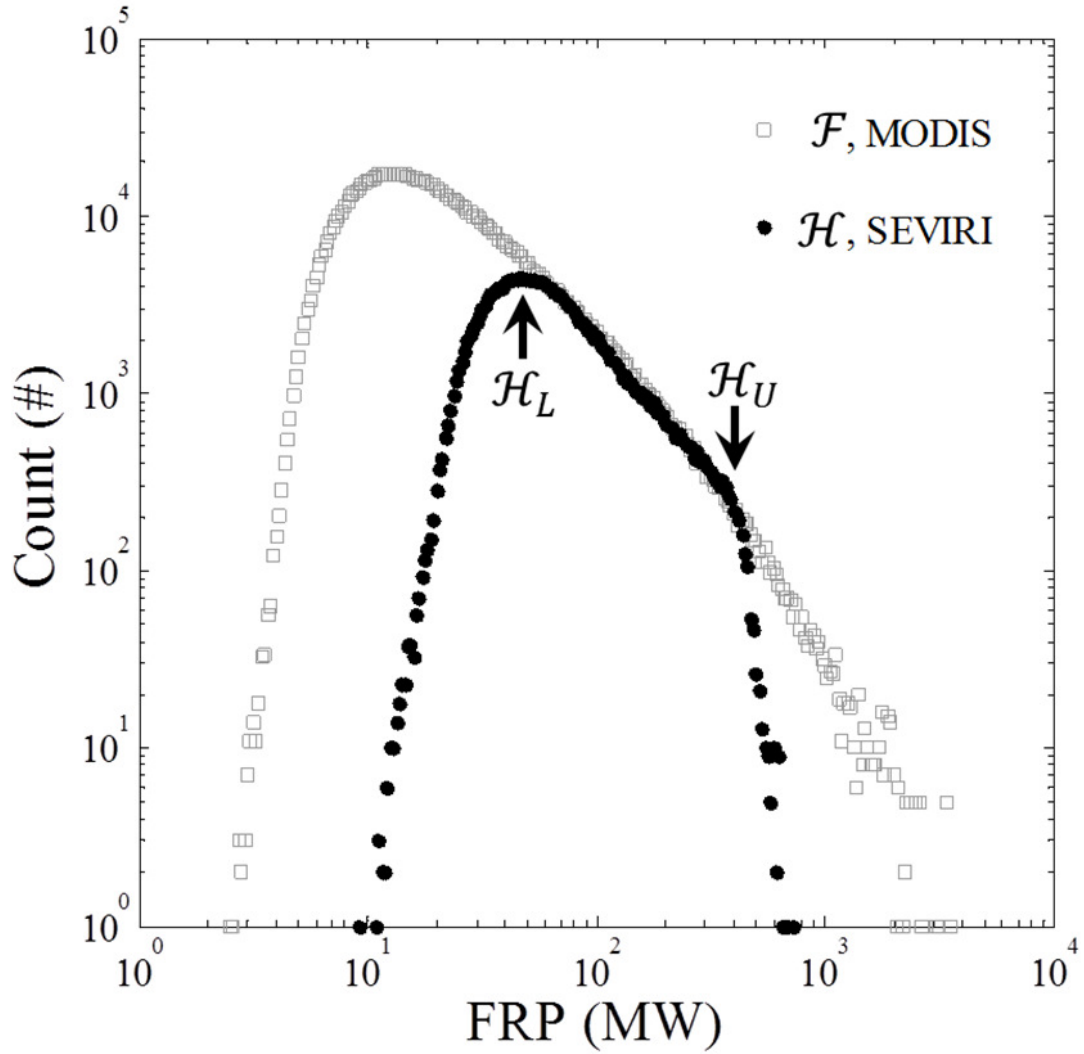


Figure 15: Frequency-magnitude distributions constructed from coincident active fire pixels detected by SEVIRI,  $\mathcal{H}$  ( $\bullet$ ) and MODIS,  $\mathcal{F}$  ( $\square$ ) over the African continent between May 2008 and May 2009. The lower breakpoint of the SEVIRI distribution,  $\mathcal{H}_L$ , coincides with the decline in SEVIRI's active fire detection performance as the thermal radiance emitted from small and/or lower intensity fires cannot be reliably distinguished from that of the background window, and so many remain undetected. The upper breakpoint,  $\mathcal{H}_U$ , coincides with the onset of IR3.9 detector saturation. The Level 3 FRP-GRID Product aims to account for the FRP that SEVIRI fails to detect as a result of these sensor artefacts, as well as by that due to cloud obscuration.

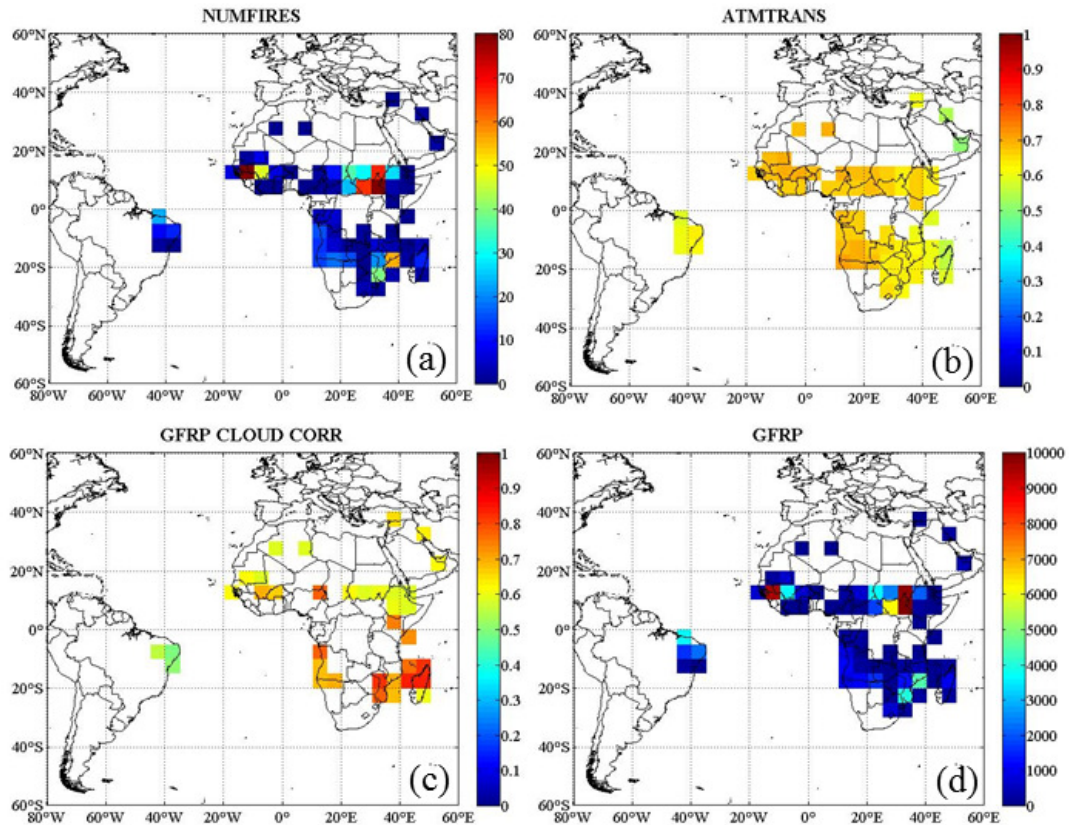


Figure 16: Example of the product contents for a single FRP-GRID product (issued hourly), as recorded on 11<sup>th</sup> November 2009 at 14:00 UTC, including (a) the average number of fires detected per 15 min imaging timeslot, (b), the average atmospheric correction factor, (c), the average cloud correction factor, and (d) an estimate of the average FRP that MODIS would have measured during the hour. A full description of all FRP-GRID product fields is provided in Table S2 in the Supplementary Materials.

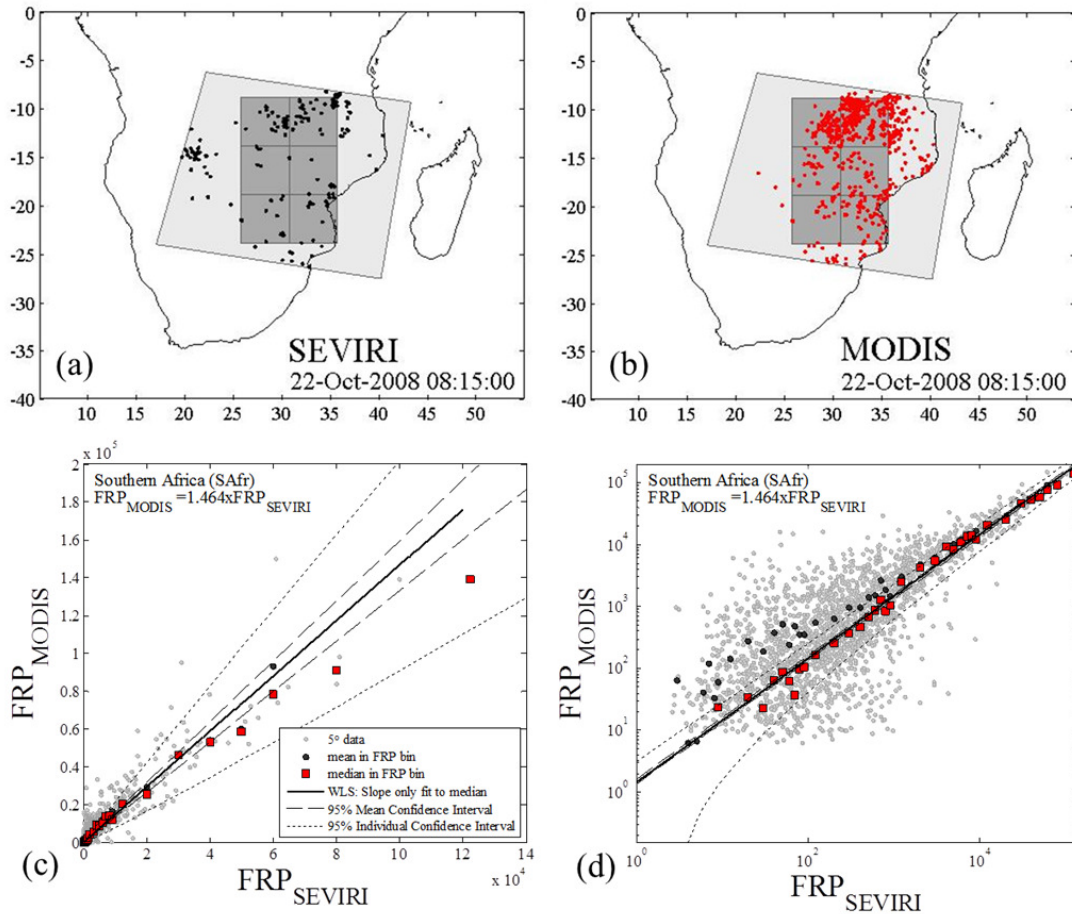


Figure 17: Illustration of the training dataset and technique used to derive the regional bias adjustment factors used in generating the FRP-GRID product, here illustrated for the southern African LSA SAF region. Temporally coincident (a) SEVIRI and (b) MODIS active fire pixels between 2008 May and 2009 May were accumulated in  $5^\circ$  grid cells strategically located within geographic areas covered by the centre two thirds of the MODIS swath. Shown is one example obtained at 08:15 UTC on 22 Oct 2008. To achieve a sufficient sample size, SEVIRI active fire pixels in  $5^\circ$  cells were averaged over an hour, as in the FRP-GRID product. These hourly values (grey circles) were binned and the result compared to the median (red squares) and mean (black circles) of the MODIS observations. Appropriate SEVIRI-to-MODIS bias adjustment coefficients were determined by performing a weighted linear least squares fit through the median values, shown in (c) on a linear scale and (d) on a log scale (here for the SAfr region only). The resulting factors are applied in the FRP-GRID processing chain.

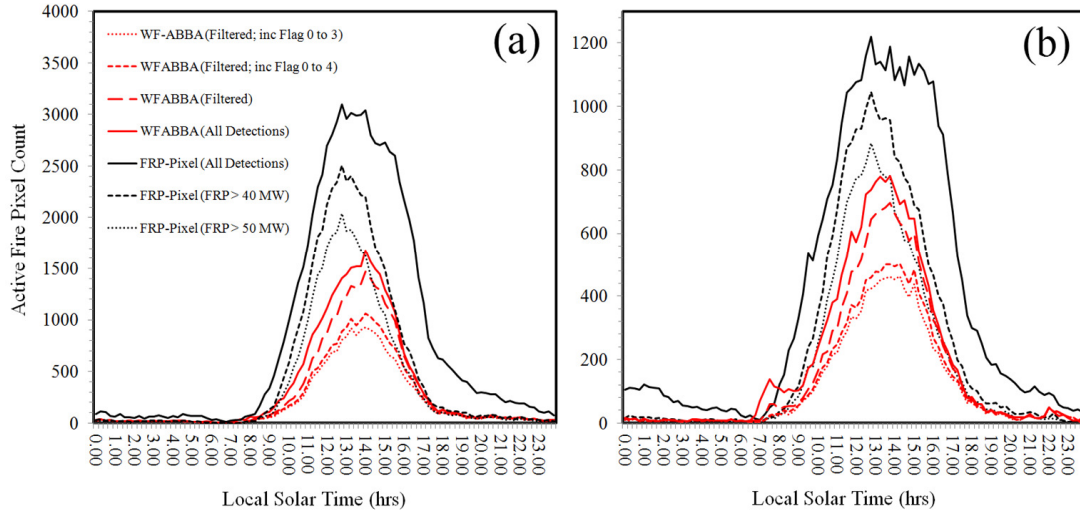


Figure 18: Comparison between FRP-PIXEL product active fire detections made across southern Africa (the LSA SAF SAfr region; Figure S1), along with those made simultaneously by the WF-ABBA SEVIRI Fire Product (Gonzalo *et al.* (2009); <http://wfabba.ssec.wisc.edu/>). Dates are (a) 2<sup>nd</sup> August 2014, and (b) 31<sup>st</sup> August 2014, and both are shown in terms of local solar time of detection. For the FRP-PIXEL product, three active fire time-series are shown, all detections; and those only from fire pixels with FRP > 40 MW and > 50 MW, since it is known that significant undercounting of active fire pixels occurs around these limits (i.e. below threshold  $\mathcal{H}_L$  in Figure 15). For the WF-ABBA active fire detections, four versions of the data are shown, all active fire detections; the WF-ABBA 'filtered' detections where SEVIRI pixels only detected as an active fire once during 24 hrs are removed; and the filtered detections keeping only the higher possibility fires (WF-ABBA flags 0 to 3) and high and medium possibility fires (WF-ABBA flags 0 to 4). Details of the WF-ABBA flags can be found at [www.ssd.noaa.gov/PS/FIRE/Layers/ABBA/abba.html](http://www.ssd.noaa.gov/PS/FIRE/Layers/ABBA/abba.html). On both days and at all timeslots, the full FRP-PIXEL product active fire record (black line) detects substantially greater numbers of active fire pixels than the full WF-ABBA record (red line), and Roberts *et al.* (2015) goes onto further compare the performance of these two products to MODIS active fire records.



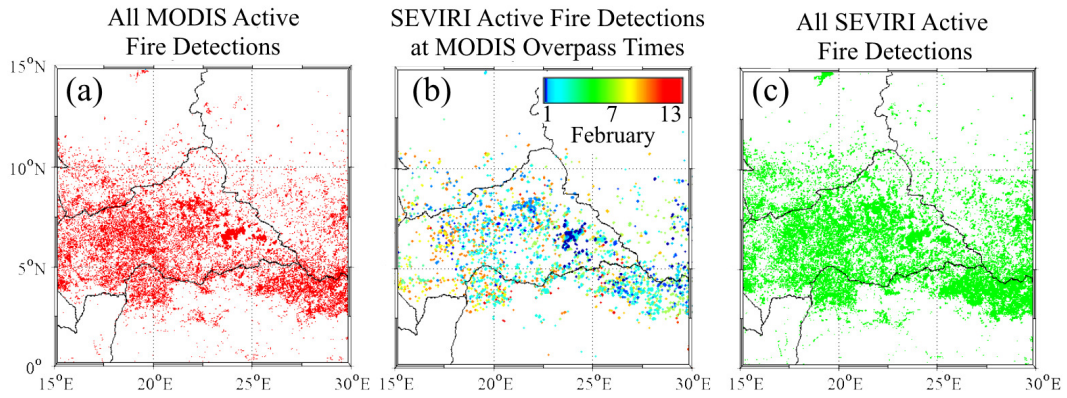


Figure 19: Active fire detections made across a  $15^{\circ} \times 15^{\circ}$  region covering Central African Republic (CAR) during a two week window (1 - 13 February 2004), as detected from (a) the MOD14/MYD14 Active Fire products, (b) SEVIRI data and the FTA algorithm within  $\pm 6$  minutes of the MODIS overpass, and (c) all SEVIRI data. In (b), the detected active fire pixels are coloured by day of detection, and it is apparent that fires appear potentially larger and are detected earlier in the east, somewhat matching the detailed analysis presented in Freeborn *et al.* (2004a, c).

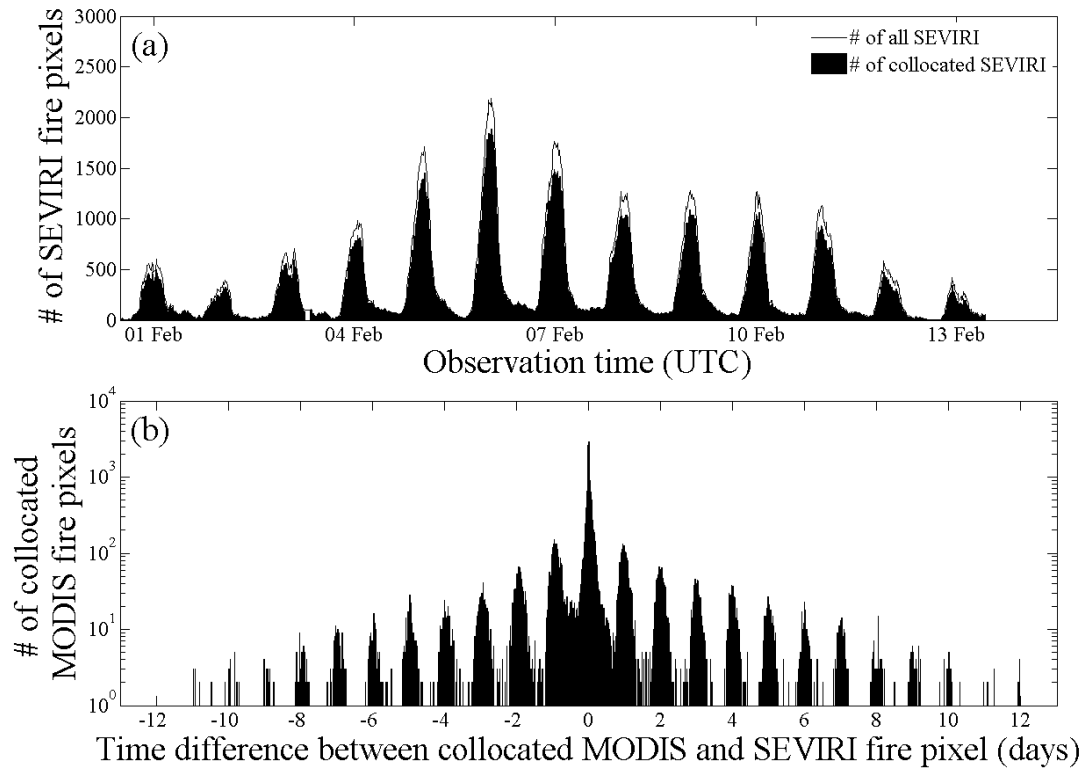


Figure 20: Results of the temporal analysis performed using the collocated SEVIRI and MODIS active fire pixels detected in Central Africa in Figure 19. (a) Total number of active fire pixels detected by the FTA algorithm in each SEVIRI timeslot, and the number that were within 4 km of a MODIS active fire pixel detected at any time during the study period. (b) Number of MODIS active fire pixels detected within 4 km of a SEVIRI fire pixel, expressed as a function of the time difference between the MODIS detection and the most contemporaneous SEVIRI active fire detection. Positive time differences represent a SEVIRI fire detection occurring after the MODIS active fire detection. Note log scale of y-axis in (b).



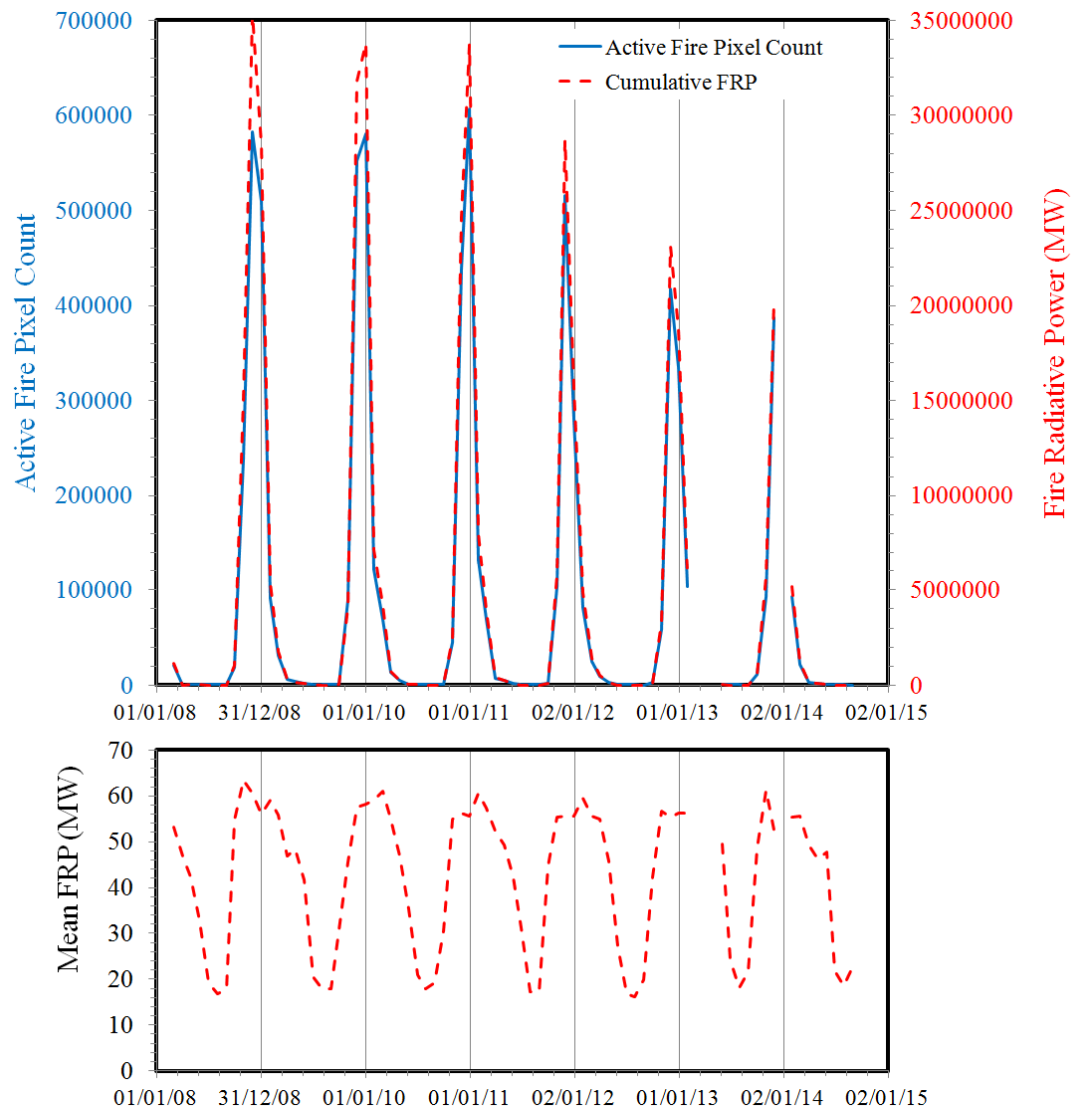


Figure 21: Metrics of monthly fire activity (total monthly FRP, monthly active fire pixel count, and the mean per-pixel FRP) for the Central African Republic (CAR), as extracted from the 2008-2014 time series of FRP-PIXEL products available from the Land Surface Analysis Satellite Applications Facility (LSA SAF; landsaf.meteo.pt).

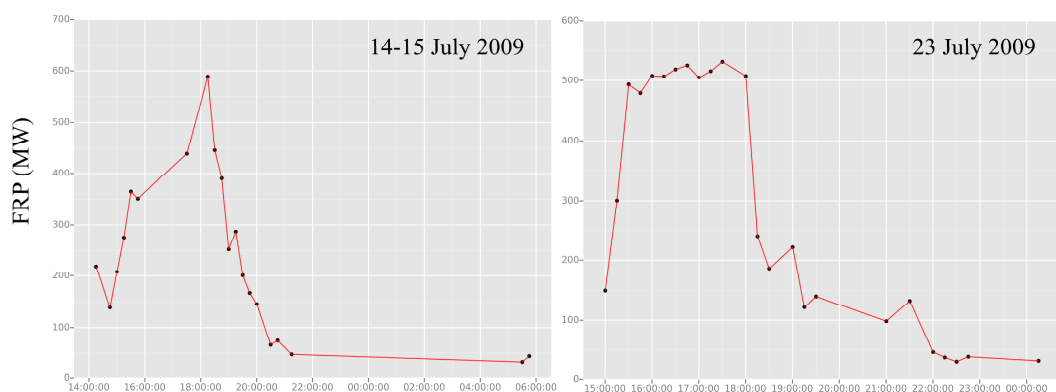
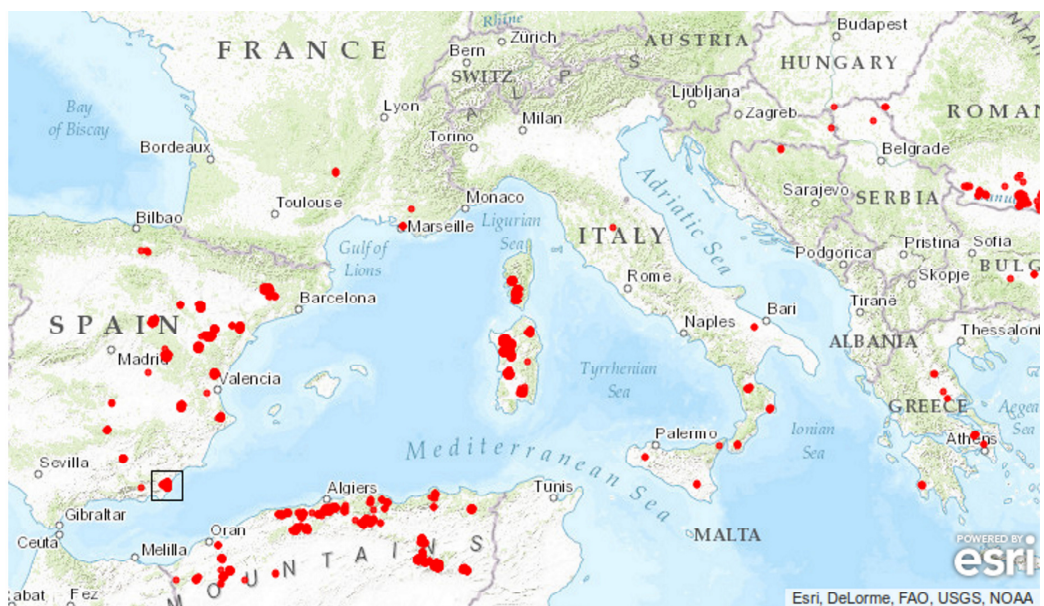


Figure 22: High FRP active fire detections made across parts of Europe and North Africa (4.0° E - 35.0° W, 25.0° N - 46.0° N) in July 2009 and stored in the SEVIRI FRP-PIXEL product. (a) Locations of active fire pixels with FRP  $\geq$  200 MW, with the location of the wildfire close to Sierra Cabrera in Spain (37.15° N, 1.92° W) is outlined, whose FRP time-series is shown in (b) and (c).